This is a repository copy of *Shear stress-driven flow : the state space of near-wall turbulence as Reτ → ∞*.

White Rose Research Online URL for this paper:
http://eprints.whiterose.ac.uk/147136/

Version: Accepted Version

Shear stress-driven flow: the state space of near-wall turbulence as $Re_\tau \to \infty$

Patrick Doohan[1]†, Ashley P. Willis[2] and Yongyun Hwang[1]

[1]Department of Aeronautics, Imperial College London, London SW7 2AZ, UK
[2]School of Mathematics and Statistics, University of Sheffield, Sheffield S3 7RH, UK

An inner-scaled, shear stress-driven flow is considered as a model of independent near-wall turbulence as $Re_\tau \to \infty$. In this limit, the model is applicable to the near-wall region and the lower part of the logarithmic layer of various parallel shear flows, including turbulent Couette flow, Poiseuille flow and Hagen-Poiseuille flow. The model is validated against damped Couette flow and there is excellent agreement between the velocity statistics and spectra for $y^+ < 40$. A near-wall flow domain of similar size to the minimal unit is analysed from a dynamical systems perspective. The edge and fifteen invariant solutions are computed, the first discovered for this flow configuration. Through continuation in the spanwise width L_z^+, the bifurcation behaviour of the solutions over the domain size is investigated. The physical properties of the solutions are explored through phase portraits, including the energy input and dissipation plane, and streak, roll and wave energy space. Finally, a Reynolds number is defined in outer units and the high-Re asymptotic behaviour of the equilibria is studied. Three lower branch solutions are found to scale consistently with vortex-wave interaction (VWI) theory, with wave forcing localising around the critical layer.

---

1. Introduction

There is an ever-growing body of experimental and numerical work on the scaling of the velocity statistics and spectra of wall-bounded turbulent flow, in both channel and pipe geometries as well as the flat-plate boundary layer. Closest to the wall, where viscous effects are dominant, the kinematic viscosity ν and local shear stress define the friction velocity u_τ and the viscous lengthscale δ_ν. One of the key observations concerning the dynamics of the near-wall region is that of the regeneration mechanism (Hamilton *et al.* 1995) or the self-sustaining process (Waleffe 1997). This is a quasi-cyclic, interactive process between streaks and quasi-streamwise vortices, in which the mean streamwise shear drives streak formation through the lift-up effect. The streaks subsequently break down due to normal mode instability or transient growth (Hamilton *et al.* 1995; Schoppa & Hussain 2002; Cassinelli *et al.* 2017) and the resulting three-dimensional wavy structure regenerates the vortices via non-linear mechanisms. The bursting time period of the near-wall self-sustaining process is $T^+ \approx 200 - 300$ (Hamilton *et al.* 1995; Jiménez *et al.* 2005), where the superscript $^+$ denotes the viscous scaling. In addition, it has been shown that there is a lower bound to the streamwise and spanwise dimensions of the

† Email address for correspondence: patrick.doohan15@imperial.ac.uk

computational domain in which turbulence can be sustained (Jiménez & Moin 1991). The dimensions of the minimal unit, which also scale in inner units, are $\lambda_x^+ \approx 250 - 350$ and $\lambda_z^+ \approx 100$, consistent with the characteristic spacing of near-wall streaks (Robinson 1991). Furthermore, it has been observed that the near-wall self-sustaining process operates independently of the outer flow and survives even when the outer structures are artificially quashed (Jiménez & Pinelli 1999). The statistics and spectra of the independent near-wall flow have been compared to that of the global flow in several previous studies (Jiménez *et al.* 2004; Hwang 2013). In particular, in the absence of the larger structures, the velocity statistics and spectra scale in inner units throughout the near-wall region (Hwang 2013).

Above the near-wall region, the flow can be decomposed into the logarithmic layer and the wake layer, the latter of which is dominated by inertial effects. The characteristic lengthscale in the logarithmic layer is y, the distance from the wall. This scaling argument was formalised in the attached eddy hypothesis (Townsend 1980), in which it was proposed that the size of the coherent structures populating the entire logarithmic layer was proportional to the distance between the eddy centre and the wall. Townsend also postulated that these coherent structures were statistically self-similar with respect to the given lengthscale. There has been a growing body of evidence in support of Townsend's theory, including the linear growth of the spanwise correlation lengthscale with distance from the wall (Tomkins & Adrian 2003), the logarithmic dependence of the turbulence intensities of the wall-parallel velocity components (Marusic *et al.* 2013) and the self-similarity of structures of various spanwise lengthscales in the logarithmic layer (Hwang 2015). Above the logarithmic layer, the velocity field structures and statistics scale in outer units, including large scale motions (Kovasznay *et al.* 1970) and very large scale motions (Kim & Adrian 1999). It has been demonstrated that the coherent structures of the logarithmic and wake layers bear a self-sustaining process remarkably similar to that of the near-wall region (Hwang & Cossu 2010; Hwang & Bengana 2016), based on the interaction between streaks and quasi-streamwise vortices. Therefore, it appears that wall-bounded turbulence is organised into a hierarchy of self-sustaining coherent structures, each of which is self-similar with respect to the characteristic inner or outer lengthscale. Furthermore, it is worth mentioning that the coherent structures populating the logarithmic and wake layers reach the near-wall region (Hutchins & Marusic 2007; Mathis *et al.* 2009; Hwang 2013; Talluru *et al.* 2014; Agostini & Leschziner 2016) and contribute significantly to the near-wall spectra at long wavelengths through scale interaction processes (Hwang 2016; Cho *et al.* 2018). These features, consistent with Townsend's theory, breach the inner-scaling of the near-wall region (Marusic *et al.* 2017) and result in the logarithmic growth of the near-wall turbulence intensities of the wall-parallel velocity components with Reynolds number (Marusic & Kunkel 2003).

The logarithmic layer can be further partitioned into lower and upper parts, depending on the relative strength of the viscous effects. The lower part, dominated by the viscous effects of the wall, is often called the 'mesolayer' (Long & Chen 1981; Afzal 1982, 1984; Sreenivasan & Sahay 1997; Wei *et al.* 2005), which has been classified using the mean momentum equation. Assuming a logarithmic mean velocity profile, it has been shown that the inner-scaled wall-normal location of maximum Reynolds stress scales with the friction Reynolds number as $y^+ \sim \sqrt{Re_\tau}$ (Long & Chen 1981; Sreenivasan & Sahay 1997; Wei *et al.* 2005), below which the viscous wall effects are not negligible. The mesolayer can therefore be more generally interpreted as the layer of fluid above the wall that scales in inner units, encompassing the entire near-wall region. Furthermore, the extent of the mesolayer increases as the friction Reynolds number increases and the flow variables scale in inner units at longer and longer wavelengths. This has been corroborated by the examination of the spectra of high-Re direct numerical simulations and the computation

of optimal perturbations with a linear theory (Hwang 2016). Therefore, if the domain size is fixed in inner units, all flow variables will also scale in inner units at a sufficiently large value of Re_τ and the near-wall contribution of the structures larger than the given domain size will be excluded.

In light of this evidence, the aim of the current study is to design and validate a model of independent near-wall turbulence at infinitely large friction Reynolds number, with regard to its location within the mesolayer. The Navier-Stokes equations are rescaled in inner units based on the kinematic viscosity and the friction velocity of the 'turbulent state', denoted by $u_{\tau,r}$. Consequently, the only model parameters are the inner-scaled computational domain dimensions (L_x^+, L_y^+, L_z^+), which remain finite even as $Re_\tau \to \infty$. At the upper boundary, a horizontally uniform shear stress is applied to maintain uniform total shear stress across the entire domain, while removing any structures above this point. At the lower boundary, a no-slip boundary condition is imposed, the distinguishing feature from previous studies in which near-wall turbulence was regarded as uniform shear flow turbulence (Lee *et al.* 1990; Sekimoto *et al.* 2016). Indeed, it has been shown recently that the statistics of near-wall turbulence are considerably different from those of uniform shear flow turbulence (Yang *et al.* 2018). The key feature of this model is that it is applicable to various parallel shear flows at sufficiently large friction Reynolds number. In this limit, the governing equations of turbulent Couette flow, Poiseuille flow and Hagen-Poiseuille flow are identical because they are essentially approximated by wall-bounded shear flow around a linear base flow. For the same reason, the model would describe the universal dynamics of the mesolayer in the absence of outer flow, as long as the domain size in all spatial directions is suitably defined.

As a first step towards studying the universal mesolayer dynamics, the well-known minimal unit of near-wall turbulence (Jiménez & Moin 1991) is considered in the present study, in which the self-sustaining process at the given inner scale is well isolated. In such a small domain, the turbulent flow is fully correlated in the streamwise and spanwise directions, and the flow dynamics are largely temporal. This contrasts with turbulence in extended domains, in which the spatial and temporal dynamics are important (see Barkley (2016) for this issue in transitional flows). Therefore, under these circumstances, the most suitable approach to analyse the shear stress-driven model is with the concepts of dynamical systems theory. The temporal evolution of a turbulent velocity field, governed by the Navier-Stokes equations, can be represented by a chaotic trajectory of an infinite dimensional dynamical system. The dynamical systems approach to turbulence emerged with the computation of the first relative equilibrium solutions (Nagata 1990; Waleffe 1998, 2001, 2003) and periodic orbits (Kawahara & Kida 2001) in channel flow. The computation of invariant solutions and their linear stability analysis allows for the construction of the state space of turbulence, within which the turbulent trajectory is confined. The laminar flow is the trivial equilibrium solution, whose linear stability may depend on the Reynolds number (Romanov 1973; Orszag 1971). The stability boundary of the laminar flow, which separates initial conditions that relaminarise from those that become fully turbulent, is referred to as the edge (Skufca *et al.* 2006; Schneider *et al.* 2008, 2007) and plays a fundamental role in structuring the state space of turbulence. The computation of invariant solutions of the Navier-Stokes equations has allowed for a simplified analysis of a number of physical processes, including an equilibrium self-sustaining process (Waleffe 1998), the self-similarity of equilibria localised in the wall-normal direction (Eckhardt & Zammert 2018) and the high-Re inner-scaling of wall-attached equilibria (Yang *et al.* 2019).

In order to study the dynamics of mesolayer turbulence, a near-wall flow domain similar in size to the minimal unit is analysed from a dynamical systems perspective. The edge

and several invariant solutions are computed, and various phase portraits explored. While invariant solutions have been reported in previous studies with a damping technique to isolate the near-wall dynamics (Jiménez & Simens 2001; Jiménez *et al.* 2005), most of the solutions presented here are new. In addition, the invariant solutions of the shear stress-driven model are valid for a multitude of parallel shear flow configurations at sufficiently large friction Reynolds number. It must also be pointed out that shear stress-driven flow is employed as a model of wind blowing over a body of water, resulting in flow structures such as Langmuir circulation (Faller 1971; Leibovich 1983; Thorpe 2004). Hence, the invariant solutions presented here are also relevant in physical oceanography. The bifurcation behaviour of the solutions over the domain size is investigated to establish connections between different solutions and to examine their physical properties. Finally, a Reynolds number is defined in outer units and the high-Re asymptotic behaviour of the equilibria is analysed to link to known high Reynolds number theories (Hall & Sherwin 2010).

2. Near-wall turbulence as $\mathrm{Re}_\tau \to \infty$

2.1. *Model formulation*

The flow considered is that of an incompressible fluid in a rectangular domain with dimensions (L_x, L_y, L_z), where x, y, z or x_1, x_2, x_3 represent the streamwise, wall-normal and spanwise coordinates, respectively. The corresponding velocity components are denoted by u, v, w or u_1, u_2, u_3 and time is denoted by t. A solid wall is located at the lower boundary of the domain at $y = 0$. Given the kinematic viscosity ν and the fluid density ρ, the instantaneous wall shear stress is defined as

$$\tau_w(t) = \rho\nu\left\langle \left.\frac{\partial u}{\partial y}\right|_{y=0} \right\rangle_{x,z}, \qquad (2.1)$$

where $\langle \ \cdot \ \rangle_{x,z}$ denotes the average in the streamwise and spanwise directions. The wall shear stress of the 'turbulent state', $\overline{\tau_w}$, is subsequently obtained from a full simulation, where $\overline{\cdot}$ denotes the average in time while the flow remains turbulent. The reference friction velocity is defined as $u_{\tau,r} = \sqrt{\overline{\tau_w}/\rho}$ and the viscous lengthscale is then defined as $\delta_\nu = \nu/u_{\tau,r}$. Using δ_ν as the characteristic lengthscale and $u_{\tau,r}$ as the characteristic velocity scale, the model is formulated in inner units with the velocity field $\mathbf{u}^+ = (u^+, v^+, w^+) = (u, v, w)/u_{\tau,r}$, spatial coordinates $\mathbf{x}^+ = (x^+, y^+, z^+) = (x, y, z)/\delta_\nu$ and time $t^+ = tu_{\tau,r}^2/\nu$. A diagram of the flow geometry is shown in figure 1.

Employing the Reynolds decomposition, the velocity field can be expressed in terms of the mean and fluctuating components

$$\mathbf{u}^+(\mathbf{x}^+, t^+) = \mathbf{U}^+(y^+) + \mathbf{u}'^+(\mathbf{x}^+, t^+), \qquad (2.2)$$

where $\mathbf{U}^+(y^+) = (U^+(y^+), 0, 0) = (\langle \overline{u^+} \rangle_{x^+,z^+}, 0, 0)$ and $\mathbf{u}'^+ = (u'^+, v'^+, w'^+)$. In channel flows, the turbulent mean and fluctuating velocity components satisfy the equations

$$\frac{dU^+}{dy^+} - \overline{\langle u'^+ v'^+ \rangle}_{x^+,z^+} = 1 - \frac{y^+}{Re_\tau} \qquad (2.3)$$

$$\mathbf{u}'^+_{t^+} + (\mathbf{U}^+ \cdot \nabla)\mathbf{u}'^+ + (\mathbf{u}'^+ \cdot \nabla)\mathbf{U}^+ = -\nabla p'^+ + \nabla^2\mathbf{u}'^+ - (\mathbf{u}'^+ \cdot \nabla)\mathbf{u}'^+ + \overline{\langle (\mathbf{u}'^+ \cdot \nabla)\mathbf{u}'^+ \rangle}_{x^+,z^+}, \qquad (2.4)$$

where p'^+ is the pressure fluctuation and the $-y^+/Re_\tau$ term is derived from the imposed pressure gradient (e.g. Townsend 1980). Within the mesolayer, the wall-normal coordinate satisfies the relation $y^+ \sim \sqrt{Re_\tau}$ (Sreenivasan & Sahay 1997; Wei *et al.* 2005).
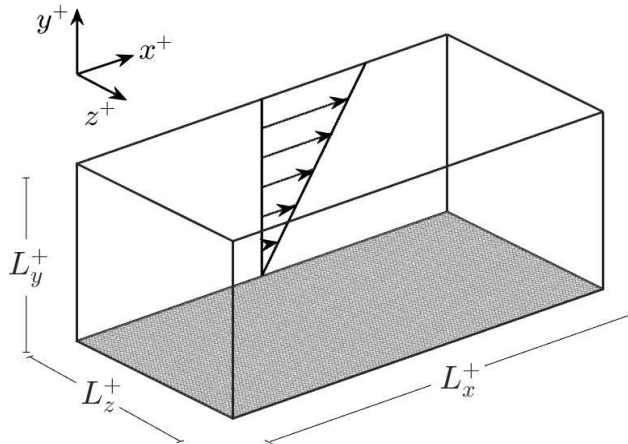
FIGURE 1. Flow geometry of the shear stress-driven model.

Therefore, as $Re_\tau \to \infty$, the $-y^+/Re_\tau$ term will vanish provided that $L_y^+ \sim \sqrt{Re_\tau}$. For parallel wall-bounded flows more generally, any terms in the mean momentum equation that are associated with the given flow geometry must vanish in the limit of $Re_\tau \to \infty$. The model is then governed by the following momentum equations for the turbulent mean and fluctuating components:

$$\frac{dU^+}{dy^+} - \overline{\langle u'^+ v'^+ \rangle}_{x^+,z^+} = 1 \qquad (2.5)$$

$$\mathbf{u}_{t^+}'^+ + (\mathbf{U}^+ \cdot \nabla)\mathbf{u}'^+ + (\mathbf{u}'^+ \cdot \nabla)\mathbf{U}^+ = -\nabla p'^+ + \nabla^2 \mathbf{u}'^+ - (\mathbf{u}'^+ \cdot \nabla)\mathbf{u}'^+ + \overline{\langle (\mathbf{u}'^+ \cdot \nabla)\mathbf{u}'^+ \rangle}_{x^+,z^+}. \qquad (2.6)$$

At the lower boundary of the domain, a no-slip condition is imposed to represent the stationary wall,

$$\mathbf{u}^+|_{y^+=0} = \mathbf{0}, \qquad (2.7)$$

whereas at the upper boundary, a horizontally uniform shear stress is applied. The uniform shear stress condition at the upper boundary is implemented such that the bulk flow rate across the domain is maintained during simulations. For this purpose, the instantaneous bulk velocity is defined as $U_b^+(t^+) = \langle u^+(x^+, y^+, z^+, t^+) \rangle_{x^+,y^+,z^+}$ ($\langle \ \cdot \ \rangle_{x^+,y^+,z^+}$ denotes the volume average) and the laminar bulk velocity is denoted by U_0^+. Then, the streamwise boundary condition is expressed as

$$\left. \frac{\partial u^+}{\partial y^+} \right|_{y^+=L_y^+} (t^+) = \left\langle \left. \frac{\partial u^+}{\partial y^+} \right|_{y^+=0} \right\rangle_{x^+,z^+} (t^+) + C^+(U_0^+ - U_b^+(t^+)), \qquad (2.8)$$

where C^+ is a tuning constant that maintains $U_b^+(t^+)$ close to U_0^+ during simulations. Given that the fluctuation of $U_b^+(t^+)$ about U_0^+ is kept to a minimum, the flow is largely independent of the value of C^+ but $C^+ \approx 0.28$ is the value used throughout the present study. Since $\overline{U_b^+(t^+)} = U_0^+$, equation (2.8) implies that the time-averaged total shear stress (i.e. the sum of molecular and Reynolds stresses) is uniform across the entire domain as long as the wall-normal velocity at the upper boundary is zero, ensuring that the mean momentum equation (2.5) is satisfied. During the simulations of the present study, $U_0^+ - U_b^+(t^+)$ has indeed been found to be very small, indicating that only a very small amount of compensation at the upper boundary is required at each time step to

maintain $U_b^+(t^+)$ close to U_0^+. This technique is very similar to that used to maintain constant mass flux in pressure-driven channel flow. At the upper boundary of the domain, impermeability and stress-free conditions are imposed for the wall-normal and spanwise velocity components respectively, namely

$$v^+|_{y^+=L_y^+} = 0 \quad \text{and} \quad \left.\frac{\partial w^+}{\partial y^+}\right|_{y^+=L_y^+} = 0, \tag{2.9}$$

ensuring zero Reynolds stress at the upper boundary. The upper boundary conditions of the model may be considered ad hoc, however, such conditions are required to ensure that the structures of the logarithmic and wake layers are safely removed. Periodic boundary conditions are imposed in both the streamwise and spanwise directions. The numerical simulations in this work were performed with the `diablo` Navier-Stokes solver (Bewley 2014). This code uses spectral methods with a 2/3 dealiasing rule in the streamwise & spanwise directions and a second-order finite difference scheme in the wall-normal direction, which has been verified extensively (e.g. Hwang 2013).

Several notable features of the present model must also be mentioned. Firstly, (2.6) does not seem to contain any explicit control parameter, such as a Reynolds number. This is essentially because the equations of motion are normalised by the viscous lengthscale δ_ν and reference friction velocity $u_{\tau,r}$. Under this rescaling, the velocity field is governed by the unit-Reynolds number Navier-Stokes equations (2.6). The inner-scaled flow variables are $O(1)$ quantities even in the limit of $Re_\tau \to \infty$. However, this does not imply that the equations do not have a control parameter. In this case, the domain dimensions (i.e. (L_x^+, L_y^+, L_z^+)) are the main control parameters, as long as they are finite. In particular, the spanwise width of the domain can be used to determine the expected multiplicity (or levels in the hierarchy) of integral lengthscales. For example, if $L_z^+ \simeq 100$, it will only include the near-wall energy-containing structures at a single integral lengthscale (Jiménez & Moin 1991). If $L_z^+ \simeq 200$, it will include two integral lengthscales (i.e. $\lambda_z^+ \simeq 100, 200$) due to the spanwise periodic boundary condition. Secondly, it must be emphasised that (2.5) only governs the turbulent mean velocity field. The laminar state (and other invariant solutions) satisfy

$$\frac{dU^+}{dy^+} - \overline{\langle u'^+ v'^+ \rangle}_{x^+,z^+} = \Delta^+, \tag{2.10}$$

where $\Delta^+ = \left.\frac{dU^+}{dy^+}\right|_{y^+=0}$ is the wall shear rate of the corresponding solution, which is smaller than unity in the laminar case. However, the present model ensures that the base flow is a uniform shear flow – this can be easily checked by setting the Reynolds stress in (2.10) to zero, with solution $U^+ = \Delta^+ y^+$. The laminar bulk velocity is then $U_0^+ = \Delta^+ L_y^+/2 \approx 13.89$. This implies that the model would be valid in the region close to the wall, where the base flow can be approximated by a uniform shear flow. This also indicates that the base flow in the mesolayer is a uniform shear flow, explaining why the description by (2.5) and (2.6) would be universal for any parallel wall-bounded shear flow. Finally, it is evident that the crucial issue in the use of the present model is the use of the upper boundary condition (2.8), which could potentially affect the region that is to be studied. For this reason, the model is first carefully validated in §2.2.

2.2. *Validation of the shear stress-driven flow model*

The shear stress-driven flow model presented in the previous subsection must now be evaluated, and the velocity statistics and spectra compared to that of independent near-wall turbulence. The obvious benchmark for the model is near-wall Couette flow,

Case	L_x^+	L_y^+	L_z^+	N_x	N_y	N_z	y_0^+
SSDF	2900	87	106	300	105	32	n/a
DCF	3042	146	111	300	161	32	95

TABLE 1. Simulation parameters of the shear stress-driven flow model and damped Couette flow.

which exactly satisfies (2.5) and (2.6) at all Reynolds numbers. In order to isolate the near-wall flow, a damping function is introduced to the system, which quashes turbulent fluctuations above a fixed wall-normal height. The damping function employed is

$$\mu^+(y^+) = \frac{\mu_0^+}{2}\left[1 + \tanh\left(10\left(\left(\frac{y^+}{y_0^+}\right)^2 - 1\right)\right)\right], \qquad (2.11)$$

similar to that used by Jiménez & Pinelli (1999). Here, μ_0^+ denotes the damping amplitude and y_0^+ denotes the damping height, such that $\mu^+(y^+)$ tends to the constant μ_0^+ above y_0^+ and decays rapidly to zero below this point. Above the damping height, the turbulent fluctuations are damped onto the mean flow, hence the system is governed by the equations

$$\mathbf{u}_{t+}^+ + (\mathbf{u}^+ \cdot \nabla)\mathbf{u}^+ = -\nabla p^+ + \nabla^2\mathbf{u}^+ - \mu^+(y^+)(\mathbf{u}^+ - \langle\mathbf{u}^+\rangle_{x^+,z^+}). \qquad (2.12)$$

The value of the damping height is chosen to be $y_0^+ \approx 95$ so that the near-wall flow is unaffected. The value of the damping amplitude must be sufficiently high to kill all turbulent fluctuations above the damping height and it was found that $\mu_0^+ \approx 0.33$ achieves appropriate results. Since the damping function kills Reynolds stresses above the damping height, the kinematic viscosity must increase in line with the FIK identity (Fukagata *et al.* 2002) to maintain similar inner-scaled domain dimensions. To compare both flow configurations, a long streamwise domain length of $L_x^+ \approx 3000$ is chosen so that the longest streaky structures are resolved. However, the spanwise domain width is chosen to be close to that of the minimal unit, $L_z^+ \approx 110$, so as to remove the wider structures of the outer flow. The shear stress-driven flow model is denoted by SSDF and damped Couette flow by DCF, and the simulation parameters are displayed in table 1. All statistics presented here were computed over a time period of $T^+ > 35000$.

The mean streamwise velocity profile of the shear stress-driven flow model compared to that of damped Couette flow is shown in figure 2. There is excellent agreement between the two flow configurations for $y^+ < 70$ but the shear stress-driven model slightly overestimates the mean velocity above this point. The viscous sublayer features the characteristic linear profile, which is also seen near the upper boundary of the domain. Similar behaviour is observed in the root mean squared velocity statistics in figure 3. The shear stress-driven model clearly captures the near-wall peak of the streamwise velocity fluctuation at $y^+ \approx 12$ but again overestimates the streamwise velocity near the upper boundary. In contrast, the wall-normal and spanwise velocity fluctuations are underestimated by the shear stress-driven model near the upper boundary but show excellent agreement closer to the wall. The premultiplied one-dimensional streamwise and spanwise wavenumber spectra are shown in figure 4. As seen in the first and second order statistics, there is excellent agreement between the shear stress-driven model and damped Couette flow for $y^+ < 40$. The streamwise wavenumber spectra
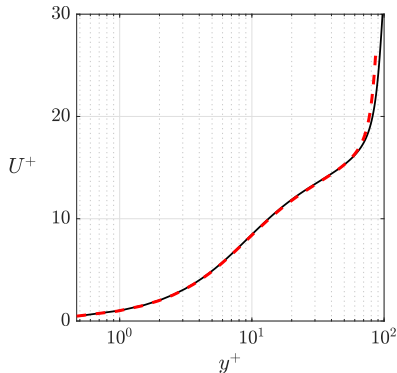
FIGURE 2. (Colour online) Mean streamwise velocity, $U^+(y^+)$, of the shear stress-driven flow model (red dashed line), plotted against that of damped Couette flow (black solid line).
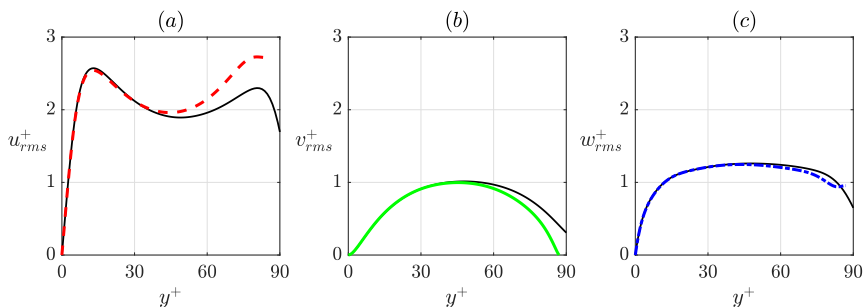

FIGURE 3. (Colour online) Root mean squared velocity of the shear stress-driven flow model; (*a*) u^+_{rms} (red dashed line), (*b*) v^+_{rms} (green solid line) and (*c*) w^+_{rms} (blue dash-dotted line), plotted against that of damped Couette flow (black solid lines).

of the streamwise velocity shows slight excitation at longer streamwise wavelengths near the upper boundary, consonant with the previous statistical results. The spectra of the wall-normal and spanwise velocity components are also underestimated near the upper boundary. In general, the spanwise wavenumber spectra of the three velocity components and Reynolds stress show excellent agreement.

3. The state space of near-wall turbulence

Having introduced the shear stress-driven flow model and validating it against damped Couette flow, the task at hand is to describe near-wall turbulence from a dynamical systems perspective. To this end, the domain dimensions are fixed at ($L_x^+ = 320, L_y^+ = 90, L_z^+ = 110$), slightly larger than the minimal unit in which turbulence can be sustained (Jiménez & Moin 1991). This reference domain is denoted by Ω and its parameters are set out in table 2. The Navier-Stokes equations, subject to boundary conditions (2.7) - (2.9), are subsequently solved in the shift-reflectional subspace,

$$[u^+, v^+, w^+](x^+, y^+, z^+) = [u^+, v^+, -w^+](x^+ + L_x^+/2, y^+, -z^+), \qquad (3.1)$$

to reduce the dimensionality of the turbulent state space. However, it has been shown that this symmetry does not significantly alter the statistics and dynamics of the turbulent trajectory (Hwang *et al.* 2016) since it captures the sinuous mode of streak
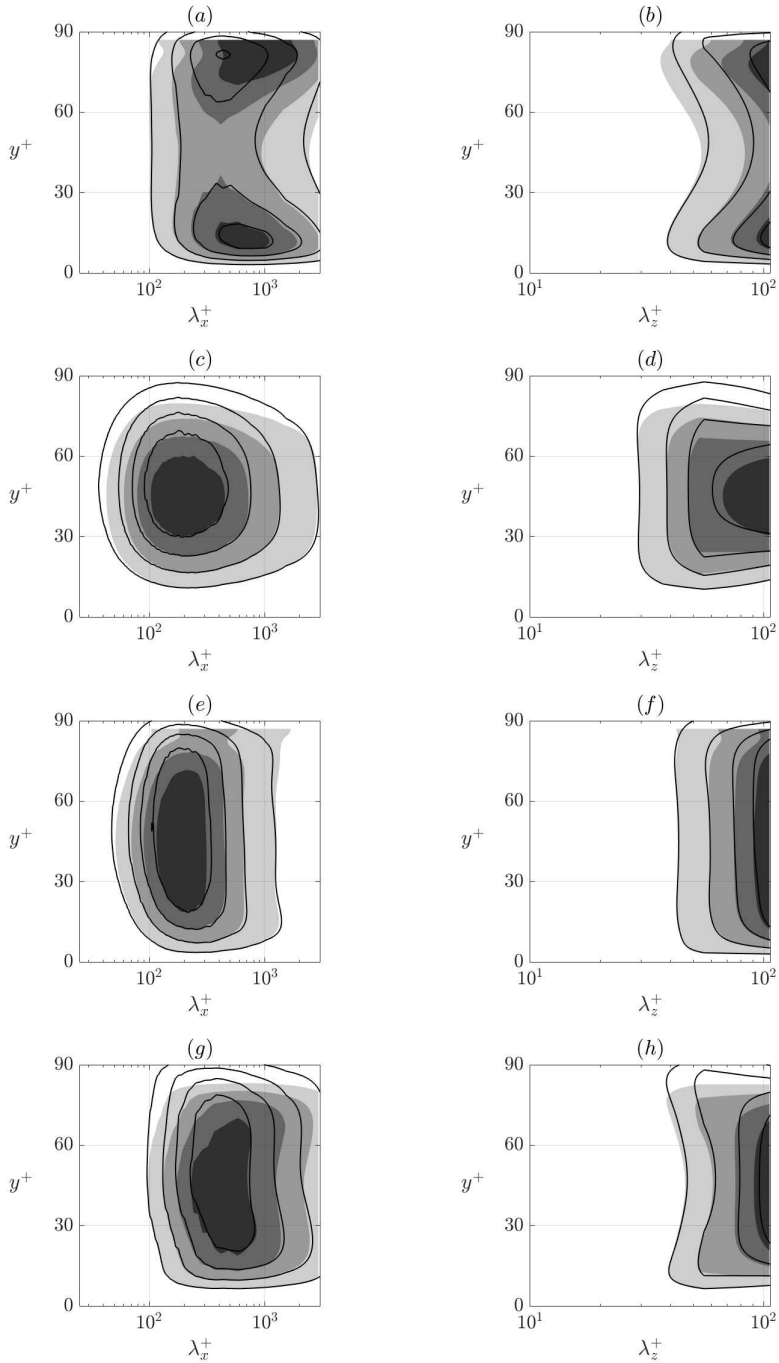
FIGURE 4. Premultiplied one-dimensional streamwise (a, c, e, g) and spanwise (b, d, f, h) wavenumber spectra of the shear stress-driven flow model; (a, b) streamwise velocity, (c, d) wall-normal velocity, (e, f) spanwise velocity and (g, h) Reynolds stress. Isocontours of damped Couette flow are superimposed in black.

L_x^+	L_y^+	L_z^+	N_x	N_y	N_z
320	90	110	32	105	32

TABLE 2. Simulation parameters of the reference domain, Ω.

instability, which is the dominant streak breakdown mechanism in the self-sustaining process (Hamilton *et al.* 1995; Cassinelli *et al.* 2017; de Giovanetti *et al.* 2017).

3.1. *Edge and invariant solutions*

As in the case of Couette flow, the base flow of the shear stress-driven flow model has a linear velocity profile. However, any perturbations to the base flow are subject to different boundary conditions than those of Couette flow, namely (2.8) and (2.9), hence the linear stability of the base flow is not guaranteed. A simple way to verify the linear stability of the base flow for the parameters chosen is to determine whether it is possible to compute the edge, the hyper-dimensional manifold that separates initial conditions that relaminarise from those that become fully turbulent (Skufca *et al.* 2006). In this case, the edge of Ω is computed via bisection, in which the turbulent fluctuations of a random initial condition are rescaled so as to lie between specific laminar and turbulent thresholds. This modified velocity field is advanced in time until the transient behaviour has decayed sufficiently, denoted by time t_0^+. The edge is a fundamental feature of the state space of a parallel wall-bounded shear flow. The turbulent state space is also structured by invariant solutions, including relative equilibrium solutions and relative periodic orbits, whose stable and unstable manifolds guide nearby turbulent trajectories. Such invariant solutions are computed using the Newton-Krylov-Hookstep algorithm (Viswanath 2007, 2009; Willis *et al.* 2013), which has been verified extensively in Hwang *et al.* (2016). Given an initial condition $\mathbf{u}_0^+$, this algorithm seeks to minimise the relative error between the initial condition and its translated time-forward map

$$r = \frac{||\mathbf{u}_0^+ - \tau(s_{x^+}, s_{z^+}) f^{T^+}(\mathbf{u}_0^+)||}{||\mathbf{u}_0^+||}, \qquad (3.2)$$

where f denotes the Navier-Stokes propagator and τ represents a translation of distance s_{x^+} in the streamwise direction and s_{z^+} in the spanwise direction. For periodic orbits, the value of T^+ is updated at each Newton iteration from a good initial guess and the converged value becomes the time period (up to positive integer multiplication of the fundamental period). For equilibria, the choice of T^+ is arbitrary but $T^+ \approx 16$ is the value used for those computed here. All invariant solutions reported in this work satisfy $r < 10^{-8}$. The eigenvalues of converged solutions are subsequently computed via Arnoldi iteration.

Defining the streamwise turbulent fluctuation energy as

$$E_u^+ = \frac{1}{2} \langle (u'^+)^2 \rangle_{x^+, y^+, z^+}, \qquad (3.3)$$

the edge of Ω as a function of time is shown in figure 5. After the transient behaviour has decayed, the edge initially shows statistically stationary behaviour, from which the first relative equilibrium solution, EQ_{A1L}, was computed. However, this equilibrium solution is unstable to a gentle relative periodic orbit on the edge. In figure 5, the edge trajectory
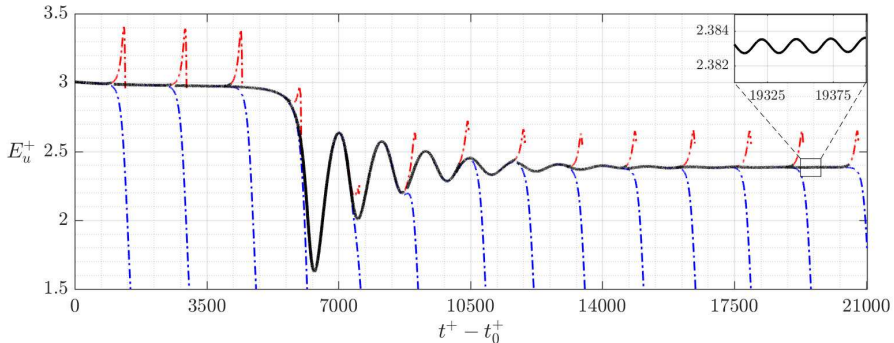
FIGURE 5. (Colour online) The edge of the reference domain Ω (black solid line), separating initial conditions that relaminarise (blue dash-dotted lines) from those that become fully turbulent (red dash-dotted lines). E_u^+ is the streamwise turbulent fluctuation energy and t_0^+ is the time by which the initial transient behaviour of the edge has decayed sufficiently. The insert shows the relative periodic orbit embedded in the edge.

leaves the neighbourhood of the equilibrium solution and is pulled towards the periodic orbit, stabilising at later time. This periodic orbit, titled PO_{A0L}, is stable on the edge and hence it is the edge state. Therefore, the transient visit of EQ_{A1L} in figure 5 is a peculiarity of the initial condition for the bisection, since any edge trajectory in the neighbourhood of PO_{A0L} will approach it monotonically. The other invariant solutions were computed using initial conditions taken directly from the turbulent trajectory or via continuation. In total, two relative periodic orbits and thirteen relative equilibrium solutions were found in Ω. They are distinguished into three distinct groups (A, B and C) in the following discussion and their properties are summarised in table 3.

The *Group A* solutions are characterised by small cross-streamwise velocity fluctuations relative to the streamwise velocity fluctuations. Velocity isosurfaces and second order statistics are shown in figure 6. Titled PO_{A0L}, EQ_{A1L}, EQ_{A2}, EQ_{A3L} and EQ_{A4L} respectively, each solution in this group is a lower branch solution (figure 9). As previously mentioned, **PO_{A0L}** is the edge state. It is time-periodic with $T^+ \approx 26.2$, an order of magnitude shorter than the bursting period of near-wall turbulence (Hamilton *et al.* 1995; Jiménez *et al.* 2005), and its oscillation amplitude is very small ($t^+ - t_0^+ \simeq 20000$ in figure 5). However, its E_u^+ value is significantly different to that of EQ_{A1L} ($t^+ - t_0^+ \simeq 0$ in figure 5), which is noticeable in the u_{rms}^+ profile near the upper boundary. This periodic orbit might be related to that identified in the near-wall region of Poiseuille flow by Jiménez & Simens (2001) or to the 'gentle' periodic orbit on the edge in Kawahara & Kida (2001) (see also Lustro *et al.* (2019)). **EQ_{A1L}** is the equilibrium solution embedded in the edge. However, it has a 3-dimensional unstable manifold; one dimension representing the instability of the edge and the other two representing its instability to PO_{A0L}. It is dominated by a pair of strong streaks, flanked by weaker vortical motion. Examination of the velocity field indicates that this is presumably the stress-driven analogue of Nagata's lower branch solution (Nagata 1990), without the shift-rotational symmetry possessed by Couette flow. If an appropriate computational domain is provided, Nagata's lower branch solution also arises as the edge state of Couette flow (Schneider *et al.* 2008). The Group A solutions all have wall shear rates well below the turbulent mean but **EQ_{A2}** is the equilibrium solution with the lowest drag in Ω (table 3). In fact, it is analogous to EQ_7 computed by Gibson *et al.* (2009) and is the only solution to comprise of two pairs of streaks. **EQ_{A3L}** is a 'wall-attached' solution, showing clear vertical localisation and

FIGURE 6. (Colour online) Velocity field visualisation and root mean squared velocity profiles of the Group A relative periodic orbit and relative equilibrium solutions, henceforth titled PO_{A0L}, EQ_{A1L}, EQ_{A2}, EQ_{A3L} and EQ_{A4L}, respectively. The red and blue surfaces represent high and low speed streaks; (a, b, d) $u^+ - \langle u^+ \rangle_{x^+, z^+} = \pm 3$, (c, e) $u^+ - \langle u^+ \rangle_{x^+, z^+} = \pm 1.5$. The yellow and green surfaces are iso-surfaces of wall-normal velocity; $v^+ = \pm 0.12$. Red dashed lines, u^+_{rms}; green solid lines, v^+_{rms}; blue dash-dotted lines, w^+_{rms}. The root mean squared velocity profile of PO_{A0L} is an average over the period T^+.

	T^+	c_x^+	Δ^+	I/I_l	E_p	$dim(W^u)$
PO_{A0L}	26.2272	14.0281	0.4053	1.3092	3.3016	1
EQ_{A1L}	-	16.8070	0.4019	1.1962	4.7462	3
EQ_{A2}	-	15.1808	0.3549	1.1325	0.5489	3
EQ_{A3L}	-	10.3307	0.3979	1.3600	1.8629	3
EQ_{A4L}	-	14.9931	0.3576	1.1423	0.8946	3
EQ_{B5L}	-	14.8210	1.0078	2.5056	20.0140	19
EQ_{B3U}	-	7.0278	0.5453	1.8650	4.0807	8
EQ_{B4U}	-	14.9599	0.4200	1.3195	2.5399	6
EQ_{B6L}	-	14.6201	0.6707	2.0041	10.7257	14
EQ_{B6U}	-	14.3803	0.7864	2.3703	12.6819	17
PO_{C0U}	25.7832	12.6168	1.1941	3.9097	14.1242	47
EQ_{C1U}	-	14.2457	1.5442	4.1139	23.5143	22
EQ_{C5U}	-	14.1047	1.6692	4.5419	23.9548	25
EQ_{C7L}	-	12.9620	1.2743	3.8623	10.3416	38
EQ_{C7U}	-	13.5580	1.6092	4.5532	13.6796	63

TABLE 3. Properties of the invariant solutions in Ω: T^+, the time period; c_x^+, the phase speed; Δ^+, the wall shear rate; I/I_l, the energy input normalised by that of the laminar state; E_p, the kinetic energy deviation from the laminar state; $dim(W^u)$, the dimension of the unstable manifold. The c_x^+, Δ^+, I/I_l and E_p values of PO_{A0L} and PO_{C0U} are averages over the period T^+.

little activity near the upper boundary. It too consists of a pair of strong streaks, driven by cross-streamwise motion an order of magnitude lower. **EQ_{A4L}** is the the last Group A solution and also exhibits vertical localisation, this time in the domain centre. The maximum streak value is similar to that of EQ_{A2}, hence it has the second-lowest drag in Ω. Again, this solution possesses a Couette flow analogue, namely EQ_3 computed by Gibson *et al.* (2009).

Group B comprises the equilibria whose wall shear rate values are in the vicinity of the turbulent mean, specifically $0.41 < \Delta^+ < 1.01$ (table 3). In this sense, these solutions can be described as 'moderately turbulent states'. In contrast to Group A, the equilibria in this group show much greater velocity field diversity, as seen in the velocity isosurfaces and second order statistics in figure 7. This is due to the fact that both lower and upper branch solutions are present. However, the Group B equilibria are clustered together in state space, as seen in the phase portraits in figures 10 and 11. In particular, the energy input (3.5) of the solutions relative to that of the laminar state lies in the interval $1.3 < I/I_l < 2.6$. These equilibria are much more unstable than the solutions of Group A, each having an unstable manifold of dimension 6 to 19. **EQ_{B5L}** is an equilibrium solution that bifurcates away from the EQ_{A1L} branch, just above the turning point (figure 9(*a*)). It is very similar structurally to a typical upper branch solution, with the localisation of the low-speed streak along the wall and high-speed streak along the upper boundary, except for significantly lower drag. In fact, the drag of this solution is almost exactly equal to that of the turbulent trajectory in Ω, hence it could be argued that EQ_{B5L} represents the mean turbulent state. **EQ_{B3U}** is the upper branch of the 'wall-attached' solution EQ_{A3L}. It consists of two distinct regions; $y^+ < 40$, where the cross-streamwise velocity fluctuations are of the same order as the streamwise fluctuations, and $y^+ > 40$,
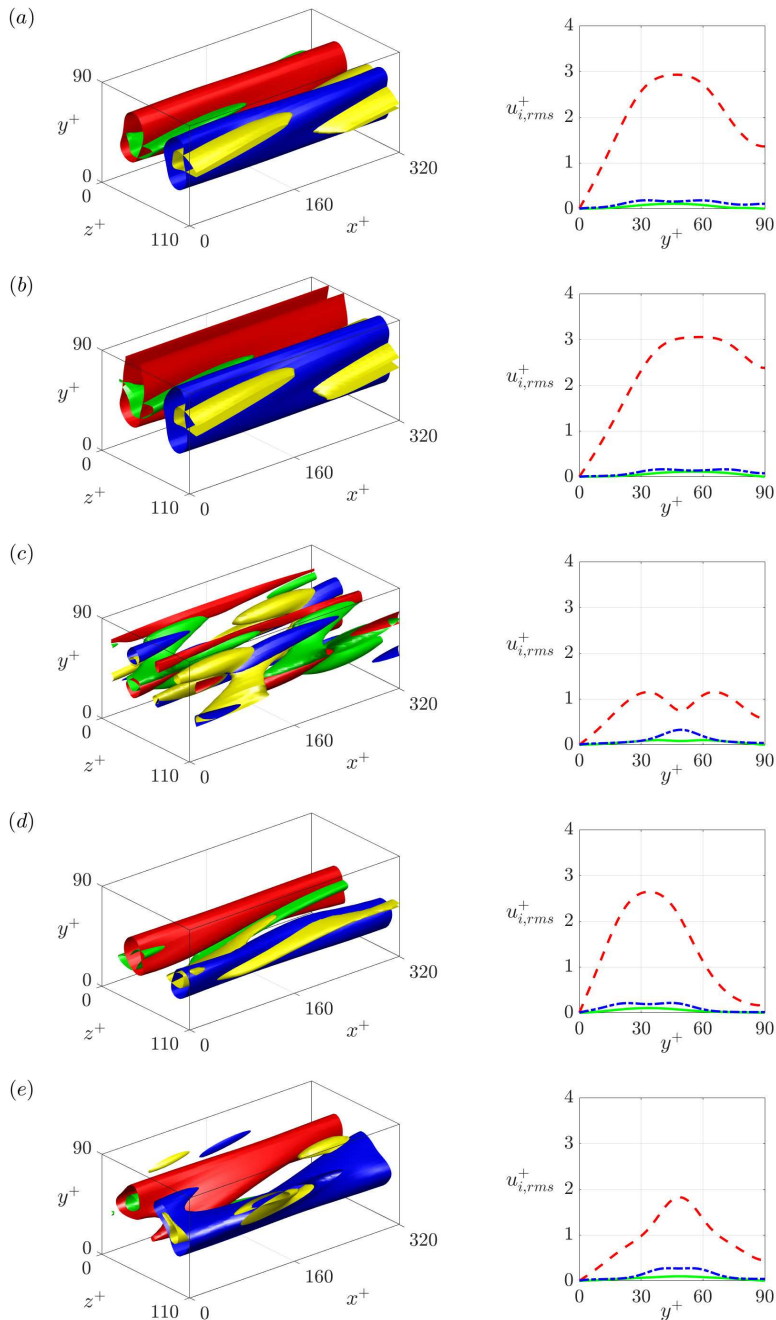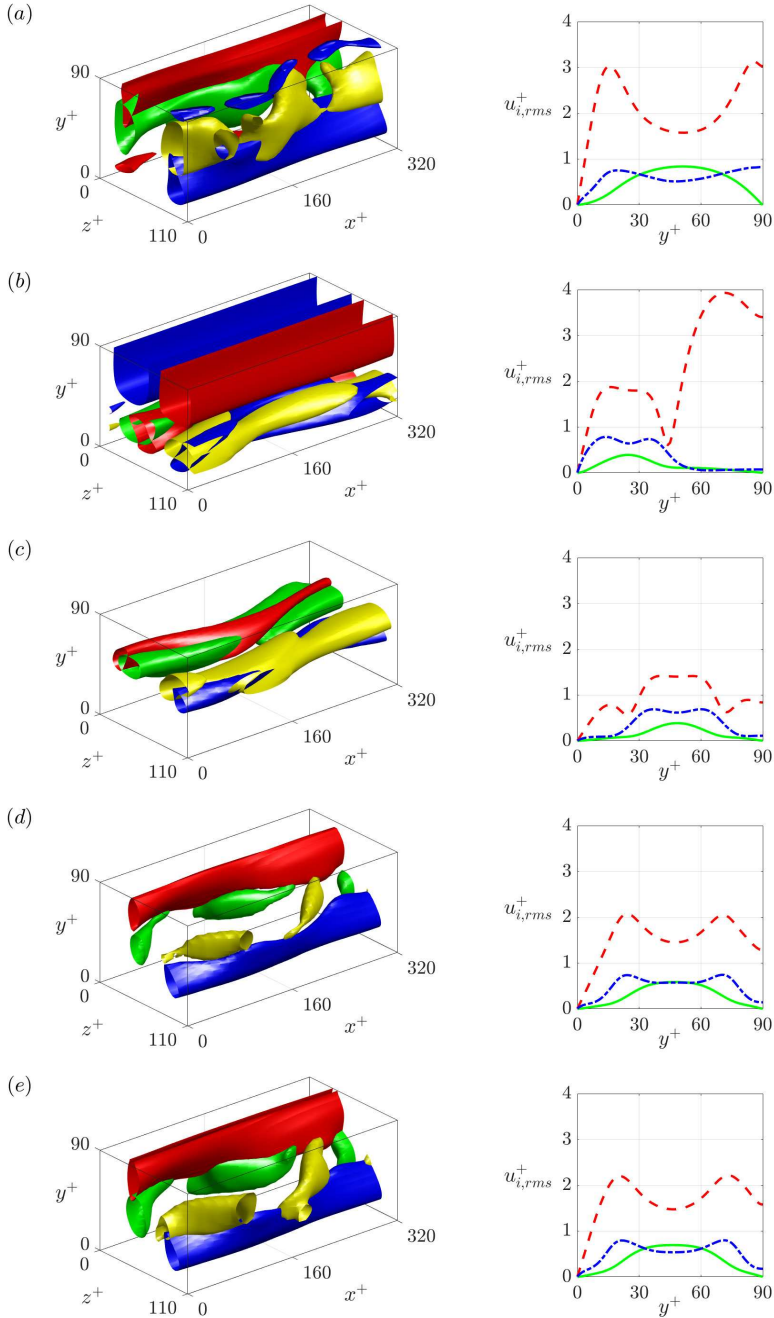
FIGURE 7. (Colour online) Velocity field visualisation and root mean squared velocity profiles of the Group B relative equilibrium solutions, henceforth titled EQ_{B5L}, EQ_{B3U}, EQ_{B4U}, EQ_{B6L} and EQ_{B6U}, respectively. The red and blue surfaces represent high and low speed streaks; (a, d, e) $u^+ - \langle u^+ \rangle_{x^+, z^+} = \pm 3$, (b, c) $u^+ - \langle u^+ \rangle_{x^+, z^+} = \pm 2$. The yellow and green surfaces are iso-surfaces of wall-normal velocity; (a, d, e) $v^+ = \pm 0.9$, (b, c) $v^+ = \pm 0.35$. Red dashed lines, u^+_{rms}; green solid lines, v^+_{rms}; blue dash-dotted lines, w^+_{rms}.

where the streamwise velocity fluctuations dominate. Correspondingly, in the velocity field visualisation (figure 7 *b*), a pair of near-wall streaks are present together with the sustaining vortical motion, as well as a pair of energetic streaks along the upper boundary. **EQ_{B4U}** is the upper branch of EQ_{A4L} and like its lower branch counterpart, it too is vertically localised in the domain centre. Both the low- and high-speed streaks exhibit wavy behaviour, resembling streak instability, and the wall-normal fluctuations are much more prominent. However, due to the wall-normal localisation, the wall shear stress remains relatively low for an upper branch solution, as for its Couette flow analogue EQ_4 (Gibson *et al.* 2009). **EQ_{B6L}** and **EQ_{B6U}** are the last Group B solutions. A lower and upper branch pair, these equilibria are positioned quite close together in state space (figures 10 and 11). Consequently, the two solutions are very similar structurally, the only differences being a shift closer to the wall in the u_{rms}^+ profile and a small increase in wall-normal velocity content.

The *Group C* solutions are characterised by large near-wall peaks in the streamwise velocity fluctuations, as shown in the velocity isosurfaces and second order statistics in figure 8. Consequently, these solutions exhibit very high wall shear rates and can be described as the 'high drag states'. In contrast to Group A and B, each of the Group C solutions has a wall shear rate greater than the turbulent mean, specifically $\Delta^+ > 1.19$ (table 3). These solutions are also highly dissipative, with energy dissipation (3.6) relative to that of the laminar state satisfying $D/D_l > 3.8$. Unsurprisingly, the solutions in this group are highly unstable, with unstable manifolds of dimension 22 or greater. **PO_{C0U}** is the upper branch of PO_{A0L}, the edge state. It is also time-periodic, with $T^+ \approx 25.8$, and its oscillation amplitude is still quite small (figures 10 and 11). In contrast to the stability of its lower branch counterpart, PO_{C0U} has a 47-dimensional unstable manifold, the second most unstable in Ω. It features very strong streaks along the upper boundary of the domain, resulting in a skewed u_{rms}^+ profile. **EQ_{C1U}** is the upper branch of EQ_{A1L}, the equilibrium solution embedded in the edge. As seen in the Group B equilibria, the low-speed streak localises along the wall and the high-speed streak localises along the upper boundary, resulting in a bimodal u_{rms}^+ distribution. Again, examination of the velocity field indicates that this is presumably the stress-driven equivalent to Nagata's upper branch solution (Nagata 1990). **EQ_{C5U}** is the upper branch of EQ_{B5L}, the solution that bifurcates away from the main EQ_{A1L} - EQ_{C1U} branch (figure 9(*a*)). Structurally, it is very similar to EQ_{C1U}, except for small differences in the wall-normal velocity content. In fact, EQ_{C5U} is the solution with the highest drag in Ω (table 3). Finally, **EQ_{C7L}** and **EQ_{C7U}** are the last Group C solutions. A lower and upper branch pair, both equilibria are characterised by very 'turbulent' velocity fields, containing high-speed streaks near the upper boundary and strong vortical structures. The root mean squared velocity profiles of both solutions are quite uneven, the only pair to exhibit such behaviour. Both equilibria are extremely unstable, possessing 38- and 63-dimensional unstable manifolds respectively.

3.2. *Bifurcation of solutions*

Thus far, three distinct groups of invariant solutions of the Navier-Stokes equations have been presented. In order to establish connections between the different solutions and to analyse their physical properties, the bifurcation of solutions over the domain size is investigated. Each periodic orbit and equilibrium solution is continued to smaller and larger values of the spanwise width L_z^+ using an arc-length continuation algorithm, while maintaining L_x^+ and L_y^+ the same. Solution curves are traced out and bifurcation
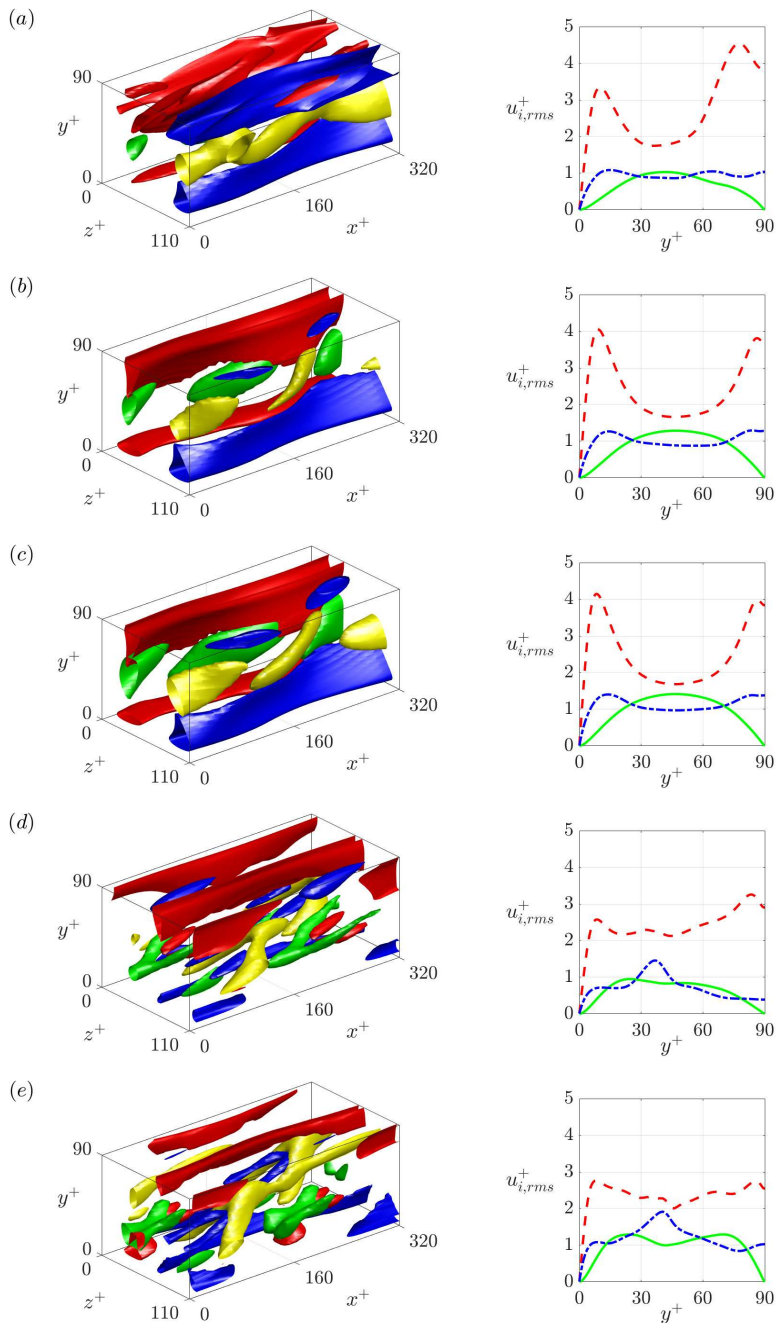
FIGURE 8. (Colour online) Velocity field visualisation and root mean squared velocity profiles of the Group C relative periodic orbit and relative equilibrium solutions, henceforth titled PO_{C0U}, EQ_{C1U}, EQ_{C5U}, EQ_{C7L} and EQ_{C7U}, respectively. The red and blue surfaces represent high and low speed streaks; $u^+ - \langle u^+ \rangle_{x^+, z^+} = \pm 3.75$. The yellow and green surfaces are iso-surfaces of wall-normal velocity; (a, d) $v^+ = \pm 1.4$, (b, c, e) $v^+ = \pm 1.9$. Red dashed lines, u^+_{rms}; green solid lines, v^+_{rms}; blue dash-dotted lines, w^+_{rms}. The root mean squared velocity profile of PO_{C0U} is an average over the period T^+.
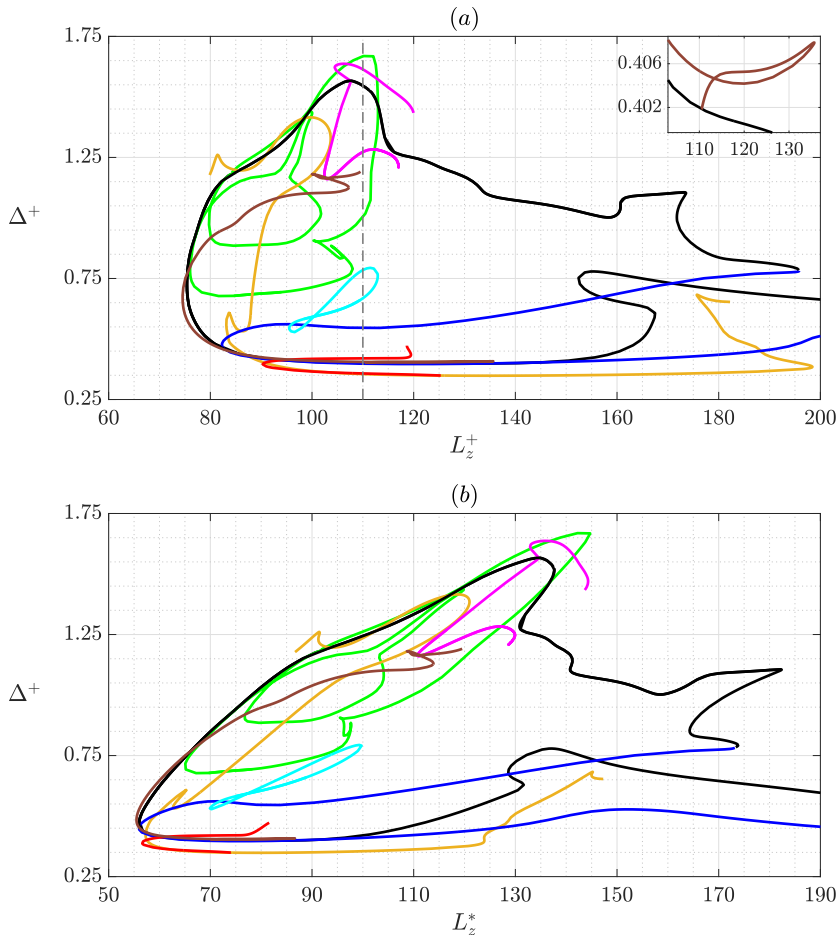
FIGURE 9. (Colour online) Wall shear rate of the invariant solutions, Δ^+, as a function of the spanwise width; (a) L_z^+ normalised by $u_{\tau,r}$, (b) L_z^* normalised by $u_{\tau,e}$. The grey dashed line represents the width of the reference domain Ω. Brown line, PO_{A0L} & PO_{C0U}; black line, EQ_{A1L} & EQ_{C1U}; gold line, EQ_{A2}; blue line, EQ_{A3L} & EQ_{B3U}; red line, EQ_{A4L} & EQ_{B4U}; green line, EQ_{B5L} & EQ_{C5U}; cyan line, EQ_{B6L} & EQ_{B6U}; pink line, EQ_{C7L} & EQ_{C7U}. The Δ^+ values of PO_{A0L} and PO_{C0U} are averages over the period T^+. The insert shows the subcritical Hopf bifurcation of EQ_{A1L}.

points are identified. The (L_z^+, Δ^+) bifurcation diagram is shown in figure 9a, where $\Delta^+ = \frac{dU^+}{dy^+}\big|_{y^+=0}$ is the wall shear rate of each solution.

In the reference domain Ω, in which $L_z^+ = 110$, PO_{A0L} is the edge state and EQ_{A1L} is the equilibrium solution embedded in the edge, as mentioned previously. Continuing PO_{A0L} to larger values of L_z^+ (in brown), it forms a saddle-node bifurcation at $L_z^+ \approx 136$ (as seen in the insert in figure 9(a)), beyond which it gains two more real unstable eigenvalues. It turns back to smaller values of L_z^+ and at $L_z^+ \approx 111$, the periodic orbit collides with the EQ_{A1L} lower branch. Analysing the eigenvalues of EQ_{A1L} reveals that it is stable on the edge for $L_z^+ > 111$ and unstable on the edge for $L_z^+ < 111$, indicating that this is a subcritical Hopf bifurcation. Continuing PO_{A0L} to smaller values of L_z^+ instead, the drag begins to increase and it forms saddle-node bifurcation at $L_z^+ \approx 74.5$, the only solution to exist at this lengthscale. Above the bifurcation point, the drag

increases substantially and after two further sharp saddle-node bifurcations, it reaches its maximum at the upper branch periodic orbit PO_{C0U}. EQ_{A1L} (in black) exhibits similar behaviour at smaller values of L_z^+, forming a saddle-node bifurcation at $L_z^+ \approx 75.5$. However, at larger values of L_z^+, the upper branch shows increasingly erratic behaviour until it turns sharply at $L_z^+ \approx 196$. The solution curve continues back down to smaller values of L_z^+, forming the upper branch on which EQ_{B3U} exists (in blue). The drag decreases through the saddle-node bifurcation point at $L_z^+ \approx 82.5$ but is largely constant in the neighbourhood of the lower branch solution, EQ_{A3L}. Clearly, there is a relationship between these two pairs of equilibrium solutions. This is reinforced by the fact that the drag of EQ_{A1L} and EQ_{A3L} is almost identical over the interval $90 < L_z^+ < 150$.

EQ_{B5L} and EQ_{C5U} are also related to the above solution pairs, as mentioned in §3.1. Just above the bifurcation point of EQ_{C1U}, the number and magnitude of unstable eigenvalues increases significantly, meaning that the upper branch is highly unstable. A secondary solution curve emerges at $L_z^+ \approx 84$ (in green), namely that of EQ_{C5U}, which is the solution with the highest drag in Ω. Just above $L_z^+ \approx 112$, there is a sharp reduction in drag before the solution curve continues back to smaller values of L_z^+ in the vicinity of the lower branch solution, EQ_{B5L}. At smaller values of L_z^+ again, this solution curve exhibits erratic 'looping' behaviour, before it eventually rejoins the EQ_{C1U} branch from which it emerged.

EQ_{A2} (in gold) is the only solution without an upper branch counterpart in Ω. The drag of the lower branch remains almost constant over the interval $100 < L_z^+ < 190$ but increases as it approaches the cusp-like saddle-node bifurcation point at $L_z^+ \approx 83$. Along the upper branch, there is a substantial increase in drag before the solution curve turns again and continues back down to smaller values of L_z^+. Below $L_z^+ \approx 80$, the residual began to increase above the desired threshold so further continuation was abandoned. In contrast, the remaining three pairs of equilibria, EQ_{A4L} & EQ_{B4U} (in red), EQ_{B6L} & EQ_{B6U} (in cyan) and EQ_{C7L} & EQ_{C7U} (in pink), are all well-defined lower and upper branch pairs. However, the solution curves of each pair differ significantly. EQ_{A4L} and EQ_{B4U} have a parabolic-shaped curve, emerging in a saddle-node bifurcation at $L_z^+ \approx 90$, even though the difference in drag between the lower and upper branches is quite small. EQ_{B6L} and EQ_{B6U} possess a unique lemniscate curve, while EQ_{C7L} and EQ_{C7U} have an almost rectangular-shaped curve. Another common feature of these three pairs of equilibria is that they only exist over a very limited interval of L_z^+, namely $90 < L_z^+ < 125$.

The bifurcation diagram in figure 9(a) also provides insight into the lengthscales of turbulent activity in the near-wall region. PO_{A0L} is the solution that exists at the smallest spanwise width, $L_z^+ \approx 74.5$, and no solutions exist below this value. As L_z^+ increases, nearly all of the equilibrium solutions are born through saddle-node bifurcations, thirteen of which exist in Ω. With the exception of EQ_{B3U}, all upper branch solutions achieve maximum drag in the interval $100 < L_z^+ < 120$, corresponding to the characteristic spacing of near-wall streaks (Robinson 1991). While the upper branch solutions are much more sensitive to the spanwise width, the lower branch solutions show little variation in drag and even quasi-constant behaviour over moderate values of L_z^+. At the largest values of L_z^+, only a few lower branch solutions still exist. As an aside, the (L_z^*, Δ^+) bifurcation diagram is shown in figure 9(b), where L_z^* is the spanwise width normalised with the friction velocity of the corresponding invariant solution, $u_{\tau,e}$. Under this rescaling, the bifurcation points of the solutions PO_{A0L}, EQ_{A1L}, EQ_{A2}, EQ_{A3L} and EQ_{A4L} coincide at $L_z^* \approx 55$, similar to that of the high-Re asymptotic state reported by Yang *et al.* (2019). The slight discrepancy is likely due to the $2:1$ aspect ratio of the horizontal computational domain (i.e. $L_x : L_z$) maintained in that work.

3.3. *Phase portraits*

Now that the connections between various invariant solutions have been determined, an approximation to the state space of near-wall turbulence can be constructed. This is the ultimate aim of the dynamical systems approach, namely how the position and stability of invariant solutions guide a chaotic turbulent trajectory through the state space. A particular phase portrait is usually chosen to exploit the inherent properties of invariant solutions or to shed light on a specific physical process. For example, if the total kinetic energy is defined as

$$E(t^+) = \frac{1}{2}\langle \mathbf{u}^+ \cdot \mathbf{u}^+ \rangle_{x^+,y^+,z^+}, \tag{3.4}$$

then its time derivative can be expressed as $\frac{dE}{dt^+} = I - D$, where

$$I(t^+) = \left\langle u^+ \left.\frac{\partial u^+}{\partial y^+}\right|_{y^+=L_y^+} \right\rangle_{x^+,z^+} \tag{3.5}$$

is the energy input and

$$D(t^+) = \left\langle \left(\frac{\partial u_i^+}{\partial x_j^+}\right)^2 \right\rangle_{x^+,y^+,z^+} \tag{3.6}$$

is the energy dissipation. However, the energy conservation property of invariant solutions implies that $\frac{dE}{dt^+}$ (or its average over the period T^+ in the case of periodic orbits) is identically zero, hence I and D (or their average over T^+) must be equal quantities. Denoting the energy input and dissipation of the laminar state by I_l and D_l respectively, the $(I/I_l, D/D_l)$ phase portrait of a turbulent trajectory and the invariant solutions is shown in figure 10(a). The invariant solutions are positioned along the diagonal, while the turbulent trajectory oscillates around it in a chaotic manner and eventually relaminarises at late time. Introducing the deviation from the laminar state $\mathbf{u}_p^+ = \mathbf{u}^+ - \mathbf{u}_l^+ = (u_p^+, v_p^+, w_p^+)$, the perturbation kinetic energy may be defined as

$$E_p(t^+) = \frac{1}{2}\langle \mathbf{u}_p^+ \cdot \mathbf{u}_p^+ \rangle_{x^+,y^+,z^+}. \tag{3.7}$$

This quantity (or its average over T^+) also remains constant for invariant solutions, thus allowing for the construction of an alternative phase portrait. The $(I/I_l, E_p)$ phase portrait of the same turbulent trajectory and the invariant solutions is shown in figure 10(b). As expected, the energy input and perturbation kinetic energy of the invariant solutions is positively correlated. The A, B and C grouping of solutions is also clearly visible in both phase portraits. The Group A solutions, represented by squares, are positioned closest to the laminar state, satisfying $I/I_l = D/D_l < 1.4$ and $E_p < 5$ (table 3). These solutions form a lower bound to the self-sustaining turbulent trajectory, consonant with the fact that PO_{A0L} is the edge state and EQ_{A1L} is embedded in the edge. In contrast, the Group C equilibria, represented by triangles, and periodic orbit are closer to the maximum values attained by the turbulent trajectory, with $I/I_l = D/D_l > 3.8$. The Group B equilibria, represented by circles, fill in the gap between the other two, closer to the mean turbulent state.

A particular phase portrait may also be chosen to investigate a specific physical process. In the case of near-wall turbulence, the relevant process is of course the self-sustaining process (Hamilton *et al.* 1995). It is therefore of interest to relate the relative equilibrium solutions and relative periodic orbits to the self-sustaining process, in order to study the state space dynamics in greater detail. In order to capture the three distinct stages, the
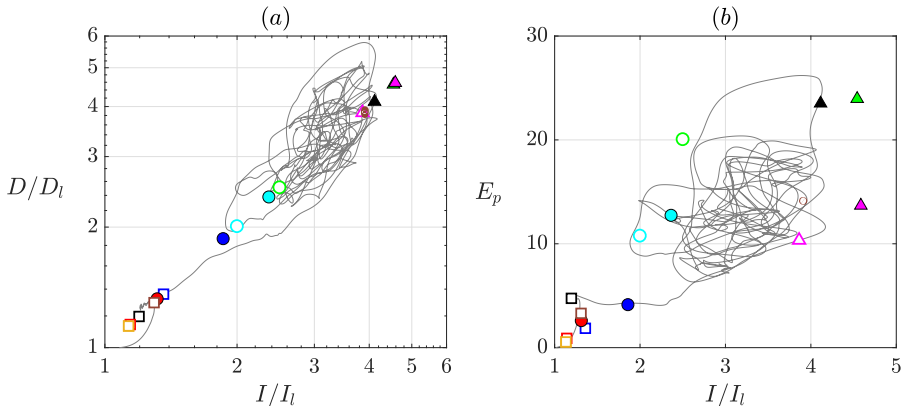
FIGURE 10. (Colour online) Phase portraits of a turbulent trajectory and the invariant solutions: (a) the $(I/I_l, D/D_l)$ plane, where I_l and D_l represent the energy input and dissipation of the laminar state; (b) the $(I/I_l, E_p)$ plane, where E_p is the kinetic energy deviation from the laminar state. Brown square & line, PO_{A0L} & PO_{C0U}; black square & triangle, EQ_{A1L} & EQ_{C1U}; gold square, EQ_{A2}; blue square & circle, EQ_{A3L} & EQ_{B3U}; red square & circle, EQ_{A4L} & EQ_{B4U}; green circle & triangle, EQ_{B5L} & EQ_{C5U}; cyan unfilled & filled circles, EQ_{B6L} & EQ_{B6U}; pink unfilled & filled triangles, EQ_{C7L} & EQ_{C7U}. The I/I_l, D/D_l and E_p values of PO_{A0L} are averages over the period T^+.

self-sustaining process will be illustrated by a three-dimensional phase portrait. Following the approach of Lucas & Kerswell (2017), the kinetic energy of the streak, roll and wave are defined as

$$E_s(t^+) = \frac{1}{2}\left\langle \langle u_p^+ \rangle_{x^+}^2 \right\rangle_{y^+,z^+}, \qquad (3.8)$$

$$E_r(t^+) = \frac{1}{2}\left\langle \langle v_p^+ \rangle_{x^+}^2 + \langle w_p^+ \rangle_{x^+}^2 \right\rangle_{y^+,z^+} \qquad (3.9)$$

and

$$E_w(t^+) = \frac{1}{2}\left\langle \left(\mathbf{u}_p^+ - \langle \mathbf{u}_p^+ \rangle_{x^+} \right)^2 \right\rangle_{x^+,y^+,z^+} \qquad (3.10)$$

respectively, such that $E_s + E_r + E_w = E_p$. Since the streak energy is of higher order than that of the roll and wave, the above quantities are normalised by their mean turbulent values in the phase portraits in figure 11. The three-dimensional portrait is shown in figure 11(a), while the two-dimensional $(E_r/\bar{E}_r, E_w/\bar{E}_w)$ and $(E_s/\bar{E}_s, E_r/\bar{E}_r)$ portraits are shown in 11(b) and 11(c) respectively. It is immediately obvious that the invariant solutions are dispersed throughout the phase portrait, indicating that the solutions have very different dynamics.

The $(E_s/\bar{E}_s, E_r/\bar{E}_r, E_w/\bar{E}_w)$ phase portrait allows for the clearest distinction between the three groups of solutions. The Group A solutions (squares) possess very little roll or wave energy, positioned almost at the origin of the $(E_r/\bar{E}_r, E_w/\bar{E}_w)$ plane. They are positioned almost along the abscissa of the $(E_s/\bar{E}_s, E_r/\bar{E}_r)$ plane, with EQ_{A1L} (the equilibrium solution embedded in the edge) showing greatest streak energy and EQ_{A2} (the solution with lowest drag) showing least. On the other hand, the high drag Group C equilibria (triangles) and periodic orbit possess the greatest roll and wave energy, corresponding to their high vorticity content. The Group B equilibria (circles) again bridge the gap, with moderately low values of both roll and wave energy. Interestingly, the Group B and C solutions are not distinguishable based on streak energy alone, given that strong streaky structures appear in the velocity field visualisations in both groups.
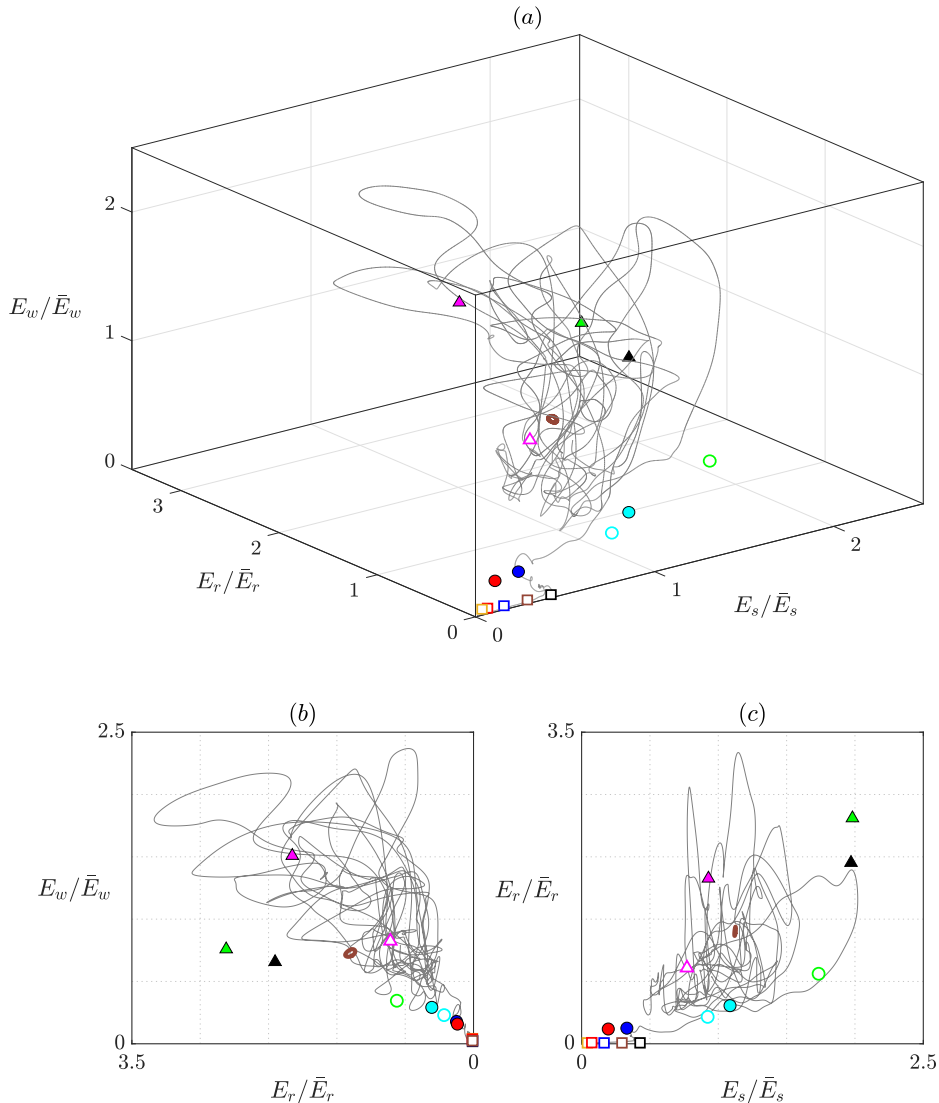
FIGURE 11. (Colour online) Phase portraits of a turbulent trajectory and the invariant solutions: (a) $(E_s/\bar{E}_s, E_r/\bar{E}_r, E_w/\bar{E}_w)$ space, where E_s, E_r and E_w represent the streak, roll and wave energy respectively, and $\overline{\cdot}$ denotes the average in time while the flow remains turbulent; (b) the $(E_r/\bar{E}_r, E_w/\bar{E}_w)$ plane; (c) the $(E_s/\bar{E}_s, E_r/\bar{E}_r)$ plane. The symbols are identical to those used in figure 10.

The above phase portraits also illustrate the interruption of the self-sustaining process and the consequent relaminarisation of the flow. At late time, the trajectory appears to escape from the turbulent state and enters the neighbourhood of the low energy states on the way to the laminar state. In particular, the trajectory appears to approach EQ_{B3U} then EQ_{A1L}, as seen in each of the $(I/I_l, D/D_l)$, $(I/I_l, E_p)$ and $(E_s/\bar{E}_s, E_r/\bar{E}_r, E_w/\bar{E}_w)$ phase portraits. However, EQ_{A1L} is the equilibrium solution embedded in the edge and other than its instability to the edge state, its only unstable eigendirection is transversal to the edge. In this case, the turbulent trajectory passes through the edge along the

unstable manifold of EQ_{A1L}, exhibiting the characteristic decay of the roll energy. The turbulent trajectory then approaches the laminar state along the E_s axis, corresponding to the slow decay of the streak energy.

It must be pointed out that each phase portrait provides a limited description of the infinite-dimensional dynamical system that is turbulence. The dynamics of turbulence that lie in dimensions orthogonal to a given phase portrait will be omitted, hence important physical processes may be missed. The $(I/I_l, D/D_l)$ and $(I/I_l, E_p)$ phase portraits shown above are not without criticism (Budanur *et al.* 2017). For example, the edge is not recognisable as the boundary between the laminar and turbulent flow regimes. Neither PO_{A0L}, the edge state, nor EQ_{A1L}, the equilibrium solution embedded in the edge, have the lowest values of I/I_l, D/D_l or E_p and several other equilibria appear to be positioned between them and the laminar state. In addition, EQ_{B4U} appears to be positioned closer to the Group A solutions, even though its velocity field is structurally very different to the solutions in that group. In order to gain a more thorough understanding of the state space of near-wall turbulence, the construction of phase portraits must be combined with the careful analysis of velocity fields, solution stability and bifurcation behaviour.

3.4. *High-Re asymptotic behaviour of equilibria*

Following the model formulation in section 2, all results presented thus far have been scaled in inner units, where the domain dimensions (L_x^+, L_y^+, L_z^+) have been the only model parameters. By the definition of the system, its Reynolds number is of order unity. In this regime, the asymptotic description should follow Deguchi (2015). Of course, the same results can be rescaled in outer units for the purpose of studying the asymptotic behaviour in the limit of vanishing viscosity. In this case, the definition of a Reynolds number is required. Using the domain height L_y as the characteristic lengthscale, the laminar bulk velocity U_0 as the characteristic velocity scale and the kinematic viscosity ν, the Reynolds number can be defined as

$$Re = \frac{L_y U_0}{\nu}. \tag{3.11}$$

In outer units, the model parameters are therefore the streamwise length of the domain L_x/L_y, the spanwise width of the domain L_z/L_y and the Reynolds number Re. In the current configuration, the values of these parameters are $L_x/L_y \approx 3.56$, $L_z/L_y \approx 1.22$ and $Re = 1250$. Given the definition of a Reynolds number, it is of interest to study the asymptotic development of the relative equilibrium solutions at high Re with L_x/L_y and L_z/L_y fixed as above. In particular, the scaling of the equilibria with Re will be examined and compared to established theories at high Reynolds number (Hall & Sherwin 2010), since this will provide valuable information about the asymptotic structure of the equilibrium solutions in the near-wall computational domain. To this end, the deviation from the laminar state $\mathbf{u}_p = (\mathbf{u} - \mathbf{u}_l)/U_0$ is reintroduced and the kinetic energy of the streak and roll are defined analogous to (3.8) and (3.9) respectively. The wave velocity field is subsequently defined as

$$(u_w, v_w, w_w) = \mathbf{u}_p - \langle \mathbf{u}_p \rangle_x \tag{3.12}$$

and the energy of the first and second streamwise modes of the wave as

$$E_{w1} = \frac{1}{2} \left\langle \hat{u}_w^2(\pm 1, y, 0) + \hat{v}_w^2(\pm 1, y, 0) + \hat{w}_w^2(\pm 1, y, 0) \right\rangle_y \tag{3.13}$$

and

$$E_{w2} = \frac{1}{2} \left\langle \hat{u}_w^2(\pm 2, y, 0) + \hat{v}_w^2(\pm 2, y, 0) + \hat{w}_w^2(\pm 2, y, 0) \right\rangle_y , \qquad (3.14)$$

where $\widehat{\cdot}$ denotes the Fourier transform.

The scaling of EQ_{A1L}, EQ_{A2}, EQ_{A3L} and EQ_{A4L} with Re is shown in figure 12, together with their upper branch counterparts EQ_{C1U}, EQ_{B3U} and EQ_{B4U}. The streak and roll energy are shown in (a, c, e, g) and the energy of the first and second streamwise modes of the wave are shown in (b, d, f, h). EQ_{A1L}, EQ_{A3L} and EQ_{A4L} all exhibit the characteristic vortex-wave interaction (VWI) scaling, where $E_s \sim Re^0$, $E_r \sim Re^{-2}$, $E_{w1} \sim Re^{-2}$ and $E_{w2} \sim Re^{-3}$ (Hall & Sherwin 2010). This result is not surprising, given that the Group A solutions possess very little roll or wave energy relative to streak energy, as seen in figure 11. EQ_{A2} exhibits similar behaviour, except that the energy of the fundamental streamwise mode of the wave is approximately zero and hence not shown. The upper branch solutions EQ_{C1U}, EQ_{B3U} and EQ_{B4U} could not be continued to as high values of the Reynolds number due to the increasing instability of equilibria at high Re. The relative equilibrium solutions not included in figure 12 either could not be continued or collided in saddle-node bifurcations at higher values of Re.

In addition to the characteristic Reynolds number scaling, VWI states are distinguishable by their velocity field structure. As shown in Hall & Sherwin (2010), the roll equations are driven by the Reynolds stresses of the wave, defined as

$$F_y = - \left\langle u_w \frac{\partial v_w}{\partial x} + v_w \frac{\partial v_w}{\partial y} + w_w \frac{\partial v_w}{\partial z} \right\rangle_x \qquad (3.15)$$

and

$$F_z = - \left\langle u_w \frac{\partial w_w}{\partial x} + v_w \frac{\partial w_w}{\partial y} + w_w \frac{\partial w_w}{\partial z} \right\rangle_x . \qquad (3.16)$$

However, in the limit of $Re \to \infty$, the wave equations become singular in the critical layer, where the mean streamwise velocity and phase speed are equal, $U(y, z) = c_x$. Hence, VWI states exhibit the localisation of the wave forcing, $F(y, z) = \sqrt{F_y^2 + F_z^2}$, around the critical layer at high Reynolds number. The critical layer position and wave forcing of EQ_{A1L}, EQ_{A2}, EQ_{A3L} and EQ_{A4L} is shown in figure 13, at $Re = 1250$ (a, c, e, g) and $Re = 12500$ (b, d, f, h). At lower Reynolds number, the wave forcing is more spatially extensive, affecting a large area surrounding the critical layer. Maximum values are attained in the critical layer with gradual spatial decay in the outer region. However, as the Reynolds number increases, the spatial extent of the wave forcing decreases and in each case, it is confined to the critical layer in the limit of $Re \to \infty$. In particular, EQ_{A2} possesses a flat critical layer, like EQ7 in Gibson *et al.* (2009) (see also Deguchi *et al.* (2013)).

EQ_{A1L}, which appears to be the analogue of Nagata's lower branch solution, has been exemplified as the canonical VWI state (Hall & Sherwin 2010). However, it has been shown above that two new equilibrium solutions exhibit VWI scaling and the localisation of wave forcing in the critical layer, namely EQ_{A3L} and EQ_{A4L}. Each of these solutions is structurally similar, with small cross-streamwise velocity fluctuations relative to streamwise velocity fluctuations. This is highlighted by the position of the Group A solutions close to the origin of the $(E_r/\bar{E}_r, E_w/\bar{E}_w)$ phase plane in figure 11(*b*). The primary difference between the three states is their wall-normal localisation, where EQ_{A3L} appears to be fully attached to the wall, EQ_{A4L} in the domain centre and EQ_{A1L}
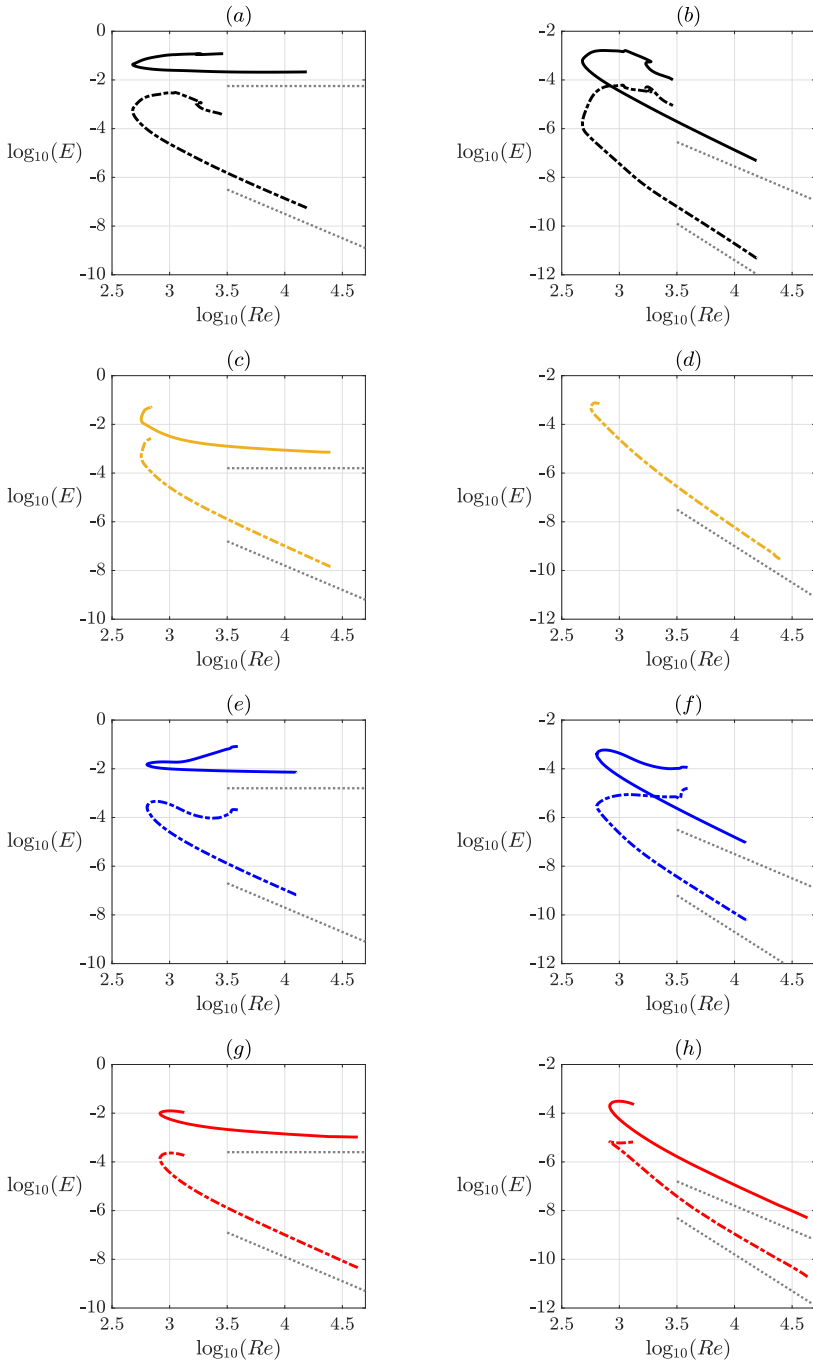
FIGURE 12. (Colour online) Scaling of (a, b) EQ_{A1L}, (c, d) EQ_{A2}, (e, f) EQ_{A3L} and (g, h) EQ_{A4L} with Re; (a, c, e, g) solid lines, E_s, dash-dotted lines, E_r; (b, d, f, h) solid lines, E_{w1}, dash-dotted lines, E_{w2}. The grey dotted lines represent the VWI scaling; $E_s \sim Re^0$, $E_r \sim Re^{-2}$, $E_{w1} \sim Re^{-2}$ and $E_{w2} \sim Re^{-3}$.
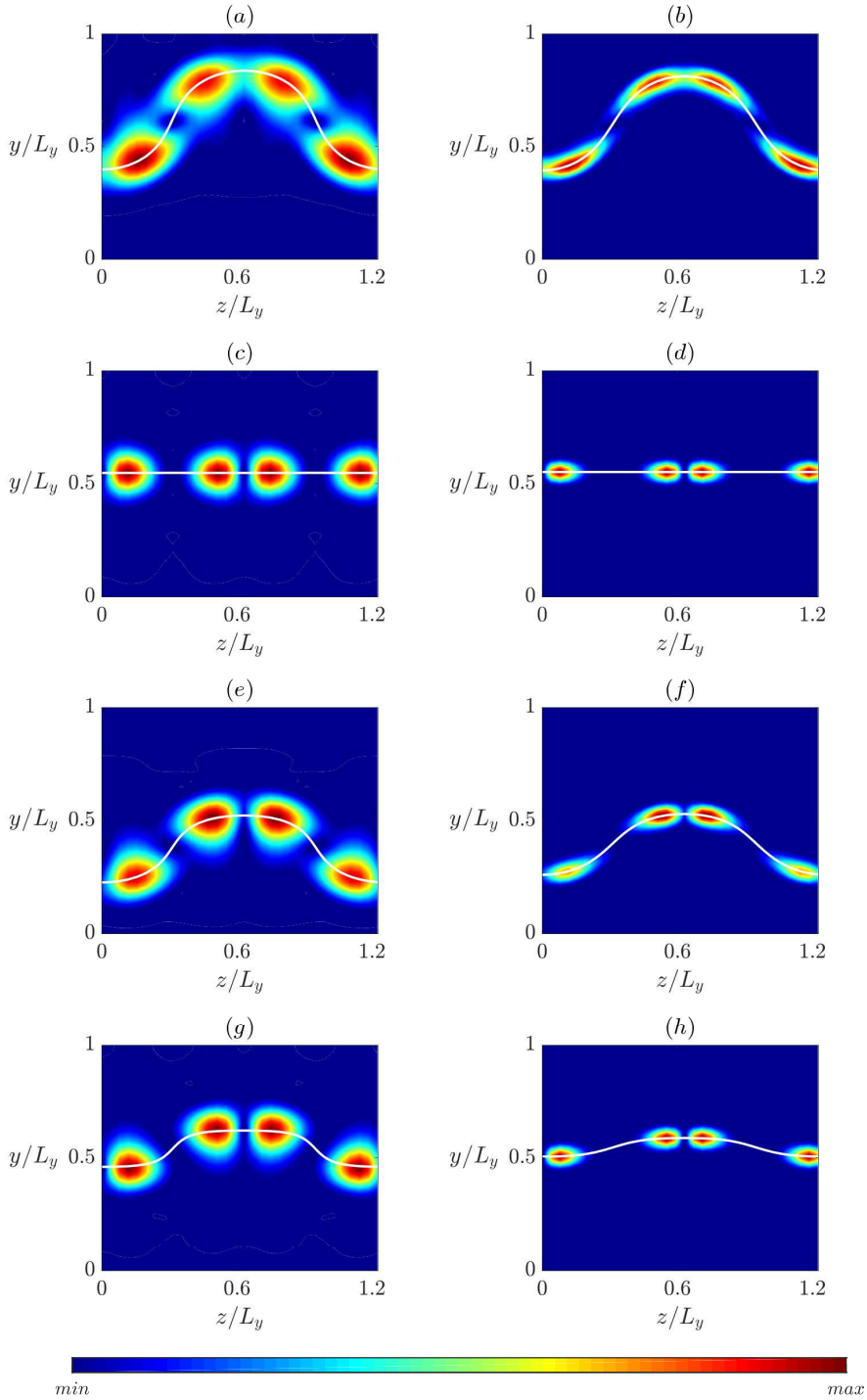
FIGURE 13. (Colour online) Wave-induced forcing, $F(y, z)$, of (a, b) EQ_{A1L}, (c, d) EQ_{A2}, (e, f) EQ_{A3L} and (g, h) EQ_{A4L}; (a, c, e, g) $Re = 1250$; (b, d, f, h) $Re = 12500$. The white line represents the critical layer position, $U(y, z) = c_x$.

along the upper boundary. The VWI states reside in the same neighbourhood of the state space of near-wall turbulence. As lower branch solutions, they are characterised by drag rates well below the turbulent mean, relatively high phase speeds and low energy input and dissipation rates (table 3). They are the most stable equilibrium solutions, each possessing three unstable eigenvalues, consonant with their position within or proximity to the edge. In addition, the VWI states are among the first solutions to emerge via saddle-node bifurcation in the (L_z^*, Δ^+) bifurcation diagram in figure 9(b). The bifurcation point appears to be $L_z^* \approx 55$, below which only the laminar state exists, indicating their relevance to the transition to turbulence.

However, it must be pointed out that the VWI states only account for a small subset of the invariant solutions presented above. Since they form a lower bound to the turbulent trajectory in terms of drag, energy input and perturbation kinetic energy, the VWI states fail to capture fully turbulent dynamics. The Group B equilibria best represent the statistics and structure of the mean turbulent state, featuring high and low speed streaks and quasi-streamwise vortices. In particular, EQ_{B5L} has wall shear rate $\Delta^+ \approx 1$ and has a similar velocity profile to that of the reference simulation (figure 3). Together with EQ_{B6U}, it appears close to the mean turbulent values of the energy input, dissipation and perturbation kinetic energy in figure 10, and streak energy in figure 11. The Group C solutions are the most 'turbulent', in the sense that they exhibit highly wavy streaks and significant vortical content. They appear to form an upper bound to the turbulent trajectory in terms of drag, energy input and dissipation and roll energy, lying close to the extremal turbulent trajectories in figures 10(a) and 11(c). Consequently, these invariant solutions are extremely unstable. For example, EQ_{C7U} is the most unstable equilibrium solution in Ω, with an incredible 63-dimensional unstable manifold, and PO_{C0U} is the most unstable periodic orbit, with a 47-dimensional unstable manifold. However, the Group C solutions are the only ones to attain wave energy values close to the turbulent mean in figure 11(b) and they also move with phase speeds $12 < c_x^+ < 14$, comparable with the advection velocity of the near-wall coherent structures observed in numerical experiments (Kim & Hussain 1993). Clearly, the solutions of Group B and C play an important role in describing the full dynamics of near-wall turbulence.

4. Conclusion

In this work, a shear stress-driven flow is introduced as a model of independent near-wall turbulence as $Re_\tau \to \infty$. The system is governed by the unit Reynolds number Navier-Stokes equations, which are valid throughout the mesolayer. A horizontally uniform shear stress is imposed at the upper boundary of the domain so as to satisfy the mean momentum equation. This model is applicable to various parallel shear flows, including turbulent Couette flow, Poiseuille flow and Hagen-Poiseuille flow, provided that $L_x^+, L_y^+, L_z^+ \sim \sqrt{Re_\tau}$. In addition, shear stress-driven flow is employed as a model of wind blowing over a body of water, hence the results presented here are also relevant in physical oceanography. The shear stress-driven flow model is validated against damped Couette flow and there is excellent agreement between the velocity statistics and spectra for $y^+ < 40$. Above this point, the mean streamwise velocity and streamwise velocity fluctuations are slightly overestimated, while the wall-normal and spanwise velocity fluctuations are slightly underestimated. Therefore, the shear stress-driven flow model can be said to describe the universal part of near-wall turbulence, which provides a means to study the flow dynamics and multiple-scale interaction unimpeded by the presence of an upper wall.

A near-wall flow domain of similar size to the minimal unit is analysed from a dynamical

systems perspective. The edge exhibits both stationary and time-periodic behaviour, from which a relative equilibrium solution and a relative periodic orbit were computed. Fifteen invariant solutions are presented in total, which can be divided into three groups based on their physical properties. Through continuation in the spanwise width L_z^+, the bifurcation behaviour of the solutions is investigated and it is found that most emerge via saddle-node bifurcations in the interval $70 < L_z^+ < 100$. Furthermore, the upper branch solutions achieve maximum wall shear rate in the interval $100 < L_z^+ < 120$, corresponding to the characteristic spacing of near-wall streaks. When the spanwise width is instead normalised by the friction velocity of the computed solution, the bifurcation points of all Group A solutions coincide at $L_z^* \approx 55$, similar to the results obtained by Yang *et al.* (2019).

The present study is analogous to that of Jiménez & Simens (2001) but with several key differences. Firstly, the shear stress-driven flow model allows for the simulation of autonomous near-wall turbulence without the need for damping functions of the form (2.11). Damped flow simulations require a greater number of grid points, many of which support only laminar flow, and the omission of these greatly improves the computational cost. Furthermore, the flow can be studied without consideration as to whether the precise form of the damping function will affect the dynamics. Secondly, the simulations in Jiménez & Simens (2001) were performed with constant volumetric flux maintained by a pressure gradient, resulting in the $-y^+/Re_\tau$ term in the mean momentum equation (2.3). Given the simulation parameters, however, this term is an $O(1)$ quantity and so the results of that study apply more directly to turbulent Poiseuille flow. Finally, the invariant solution in Jiménez & Simens (2001) is not computed explicitly and is only identifiable at low values of the mask height δ_1^+. Above $\delta_1^+ \approx 70$, only chaotic turbulent flow is observed, in contrast to the fifteen explicitly-computed invariant solutions presented in the current work for wall-normal domain height $L_y^+ = 90$.

The computation of the invariant solutions of the shear stress-driven flow model and their linear stability analysis allows for the construction of the state space of near-wall turbulence. The chaotic turbulent trajectory and invariant solutions are visualised in several phase portraits, including the energy input and dissipation plane, and streak, roll and wave energy space. The Group A solutions, three of which exhibit the characteristic vortex-wave interaction scaling at high-Re, are characterised by low energy input and dissipation rates, relatively high phase speeds and few unstable eigenvalues, consonant with their proximity to the edge. While the Group A solutions form a lower bound to the turbulent trajectory, the Group B equilibria best represent the statistics and structure of the mean turbulent state, featuring high and low speed streaks and quasi-streamwise vortices. The Group C solutions appear to form an upper bound to the turbulent trajectory in terms of drag, energy input and dissipation and roll energy, and hence are extremely unstable. Though they do not exist at high values of Re, the Group B and C solutions play an important role in describing the full dynamics of near-wall turbulence.

The statistical results and invariant solutions presented in this work have all been computed in minimal ($L_z^+ \approx 110$) near-wall ($L_y^+ \approx 90$) flow domains, which only allow for the simulation of near-wall energy-containing structures at a single integral lengthscale (Jiménez & Moin 1991). However, the extent of the mesolayer increases as the friction Reynolds number increases as $y_{max}^+ \sim \sqrt{Re_\tau}$, meaning that at extremely high Reynolds numbers, the mesolayer encompasses a hierarchy of scales – not just one. Therefore, the governing equations (2.5,2.6) are valid for arbitrary values of the domain dimensions (L_x^+, L_y^+, L_z^+), under the assumption that the friction Reynolds number is sufficiently high. Once the spanwise width of the domain exceeds $L_z^+ \simeq 200$, then energy-containing

structures at two integral lengthscales ($\lambda_z^+ \simeq 100, 200$) will be present, due to the periodic boundary condition in the spanwise direction. In such a flow domain, the interaction between the large and small scale structures will alter the turbulent dynamics, in contrast to the isolated single-scale turbulence analysed here. This study is only the first step in the investigation of multiscale mesolayer turbulence.

<div align="center">REFERENCES</div>

AFZAL, NOOR 1982 Fully developed turbulent flow in a pipe: an intermediate layer. *Ingenieur-Archiv* **52** (6), 355–377.

AFZAL, NOOR 1984 Mesolayer theory for turbulent flows. *AIAA journal* **22** (3), 437–439.

AGOSTINI, LIONEL & LESCHZINER, MICHAEL 2016 Predicting the response of small-scale near-wall turbulence to large-scale outer motions. *Physics of Fluids* **28** (1), 015107.

BARKLEY, DWIGHT 2016 Theoretical perspective on the route to turbulence in a pipe. *Journal of Fluid Mechanics* **803**.

BEWLEY, TR 2014 *Numerical Renaissance: Simulation, Optimization and Control*. Renaissance Press.

BUDANUR, NAZMI BURAK, SHORT, KIMBERLY Y, FARAZMAND, MOHAMMAD, WILLIS, ASHLEY P & CVITANOVIĆ, PREDRAG 2017 Relative periodic orbits form the backbone of turbulent pipe flow. *Journal of Fluid Mechanics* **833**, 274–301.

CASSINELLI, ANDREA, DE GIOVANETTI, MATTEO & HWANG, YONGYUN 2017 Streak instability in near-wall turbulence revisited. *Journal of Turbulence* **18** (5), 443–464.

CHO, MINJEONG, HWANG, YONGYUN & CHOI, HAECHEON 2018 Scale interactions and spectral energy transfer in turbulent channel flow. *Journal of Fluid Mechanics* **854**, 474–504.

DEGUCHI, KENGO 2015 Self-sustained states at kolmogorov microscale. *Journal of Fluid Mechanics* **781**.

DEGUCHI, KENGO, HALL, PHILIP & WALTON, ANDREW 2013 The emergence of localized vortex–wave interaction states in plane couette flow. *Journal of Fluid Mechanics* **721**, 58–85.

ECKHARDT, BRUNO & ZAMMERT, STEFAN 2018 Small scale exact coherent structures at large reynolds numbers in plane couette flow. *Nonlinearity* **31** (2), R66.

FALLER, ALAN J 1971 Oceanic turbulence and the langmuir circulations. *Annual Review of Ecology and Systematics* **2** (1), 201–236.

FUKAGATA, KOJI, IWAMOTO, KAORU & KASAGI, NOBUHIDE 2002 Contribution of reynolds stress distribution to the skin friction in wall-bounded flows. *Physics of Fluids* **14** (11), L73–L76.

GIBSON, JOHN F, HALCROW, JONATHAN & CVITANOVIĆ, PREDRAG 2009 Equilibrium and travelling-wave solutions of plane couette flow. *Journal of Fluid Mechanics* **638**, 243–266.

DE GIOVANETTI, MATTEO, SUNG, HYUNG JIN & HWANG, YONGYUN 2017 Streak instability in turbulent channel flow: the seeding mechanism of large-scale motions. *Journal of Fluid Mechanics* **832**, 483–513.

HALL, PHILIP & SHERWIN, SPENCER 2010 Streamwise vortices in shear flows: harbingers of transition and the skeleton of coherent structures. *Journal of Fluid Mechanics* **661**, 178–205.

HAMILTON, JAMES M, KIM, JOHN & WALEFFE, FABIAN 1995 Regeneration mechanisms of near-wall turbulence structures. *Journal of Fluid Mechanics* **287**, 317–348.

HUTCHINS, NICHOLAS & MARUSIC, IVAN 2007 Large-scale influences in near-wall turbulence. *Philosophical Transactions of the Royal Society of London A: Mathematical, Physical and Engineering Sciences* **365** (1852), 647–664.

HWANG, YONGYUN 2013 Near-wall turbulent fluctuations in the absence of wide outer motions. *Journal of Fluid Mechanics* **723**, 264–288.

HWANG, YONGYUN 2015 Statistical structure of self-sustaining attached eddies in turbulent channel flow. *Journal of Fluid Mechanics* **767**, 254–289.

HWANG, YONGYUN 2016 Mesolayer of attached eddies in turbulent channel flow. *Physical Review Fluids* **1** (6), 064401.

HWANG, YONGYUN & BENGANA, YACINE 2016 Self-sustaining process of minimal attached eddies in turbulent channel flow. *Journal of Fluid Mechanics* **795**, 708–738.

HWANG, YONGYUN & COSSU, CARLO 2010 Self-sustained process at large scales in turbulent channel flow. *Physical review letters* **105** (4), 044505.

HWANG, YONGYUN, WILLIS, ASHLEY P & COSSU, CARLO 2016 Invariant solutions of minimal large-scale structures in turbulent channel flow for Re_τ up to 1000. *Journal of Fluid Mechanics* **802**.

JIMÉNEZ, JAVIER, DEL ALAMO, JUAN C & FLORES, OSCAR 2004 The large-scale dynamics of near-wall turbulence. *Journal of Fluid Mechanics* **505**, 179–199.

JIMÉNEZ, JAVIER, KAWAHARA, GENTA, SIMENS, MARK P, NAGATA, MASATO & SHIBA, MAKOTO 2005 Characterization of near-wall turbulence in terms of equilibrium and "bursting" solutions. *Physics of Fluids* **17** (1), 015105.

JIMÉNEZ, JAVIER & MOIN, PARVIZ 1991 The minimal flow unit in near-wall turbulence. *Journal of Fluid Mechanics* **225**, 213–240.

JIMÉNEZ, JAVIER & PINELLI, ALFREDO 1999 The autonomous cycle of near-wall turbulence. *Journal of Fluid Mechanics* **389**, 335–359.

JIMÉNEZ, JAVIER & SIMENS, MARK P 2001 Low-dimensional dynamics of a turbulent wall flow. *Journal of Fluid Mechanics* **435**, 81–91.

KAWAHARA, GENTA & KIDA, SHIGEO 2001 Periodic motion embedded in plane couette turbulence: regeneration cycle and burst. *Journal of Fluid Mechanics* **449**, 291–300.

KIM, JOHN & HUSSAIN, FAZLE 1993 Propagation velocity of perturbations in turbulent channel flow. *Physics of Fluids A: Fluid Dynamics* **5** (3), 695–706.

KIM, KC & ADRIAN, RJ 1999 Very large-scale motion in the outer layer. *Physics of Fluids* **11** (2), 417–422.

KOVASZNAY, LESLIE SG, KIBENS, VALDIS & BLACKWELDER, RON F 1970 Large-scale motion in the intermittent region of a turbulent boundary layer. *Journal of Fluid Mechanics* **41** (2), 283–325.

LEE, MOON JOO, KIM, JOHN & MOIN, PARVIZ 1990 Structure of turbulence at high shear rate. *Journal of Fluid Mechanics* **216**, 561–583.

LEIBOVICH, SIDNEY 1983 The form and dynamics of langmuir circulations. *Annual Review of Fluid Mechanics* **15** (1), 391–427.

LONG, ROBERT R & CHEN, TIEN-CHAY 1981 Experimental evidence for the existence of the 'mesolayer' in turbulent systems. *Journal of Fluid Mechanics* **105**, 19–59.

LUCAS, DAN & KERSWELL, RICH 2017 Sustaining processes from recurrent flows in body-forced turbulence. *Journal of Fluid Mechanics* **817**.

LUSTRO, JULIUS RHOAN T, KAWAHARA, GENTA, VAN VEEN, LENNAERT, SHIMIZU, MASAKI & KOKUBU, HIROSHI 2019 The onset of transient turbulence in minimal plane couette flow. *Journal of Fluid Mechanics* **862**.

MARUSIC, IVAN, BAARS, WOUTIJN J & HUTCHINS, NICHOLAS 2017 Scaling of the streamwise turbulence intensity in the context of inner-outer interactions in wall turbulence. *Physical Review Fluids* **2** (10), 100502.

MARUSIC, IVAN & KUNKEL, GARY J 2003 Streamwise turbulence intensity formulation for flat-plate boundary layers. *Physics of Fluids* **15** (8), 2461–2464.

MARUSIC, IVAN, MONTY, JASON P, HULTMARK, MARCUS & SMITS, ALEXANDER J 2013 On the logarithmic region in wall turbulence. *Journal of Fluid Mechanics* **716**.

MATHIS, ROMAIN, HUTCHINS, NICHOLAS & MARUSIC, IVAN 2009 Large-scale amplitude modulation of the small-scale structures in turbulent boundary layers. *Journal of Fluid Mechanics* **628**, 311–337.

NAGATA, M 1990 Three-dimensional finite-amplitude solutions in plane couette flow: bifurcation from infinity. *Journal of Fluid Mechanics* **217**, 519–527.

ORSZAG, STEVEN A 1971 Accurate solution of the orr–sommerfeld stability equation. *Journal of Fluid Mechanics* **50** (4), 689–703.

ROBINSON, STEPHEN K 1991 Coherent motions in the turbulent boundary layer. *Annual Review of Fluid Mechanics* **23** (1), 601–639.

ROMANOV, VALERII ALEKSANDROVICH 1973 Stability of plane-parallel couette flow. *Functional analysis and its applications* **7** (2), 137–146.

SCHNEIDER, TOBIAS M, ECKHARDT, BRUNO & YORKE, JAMES A 2007 Turbulence transition and the edge of chaos in pipe flow. *Physical review letters* **99** (3), 034502.

SCHNEIDER, TOBIAS M, GIBSON, JOHN F, LAGHA, MAHER, DE LILLO, FILIPPO & ECKHARDT,

Bruno 2008 Laminar-turbulent boundary in plane couette flow. *Physical Review E* **78** (3), 037301.

Schoppa, W & Hussain, Fazle 2002 Coherent structure generation in near-wall turbulence. *Journal of fluid Mechanics* **453**, 57–108.

Sekimoto, Atsushi, Dong, Siwei & Jiménez, Javier 2016 Direct numerical simulation of statistically stationary and homogeneous shear turbulence and its relation to other shear flows. *Physics of Fluids* **28** (3), 035101.

Skufca, Joseph D, Yorke, James A & Eckhardt, Bruno 2006 Edge of chaos in a parallel shear flow. *Physical review letters* **96** (17), 174101.

Sreenivasan, Katepalli R & Sahay, Anupam 1997 The persistence of viscous effects in the overlap region, and the mean velocity in turbulent pipe and channel flows. In *Self-Sustaining Mechanisms of Wall Turbulence* (ed. Ronald Panton), pp. 253–272. Southampton, UK: Computational Mechanics Publications.

Talluru, KM, Baidya, R, Hutchins, N & Marusic, Ivan 2014 Amplitude modulation of all three velocity components in turbulent boundary layers. *Journal of Fluid Mechanics* **746**.

Thorpe, SA 2004 Langmuir circulation. *Annu. Rev. Fluid Mech.* **36**, 55–79.

Tomkins, Christopher D & Adrian, Ronald J 2003 Spanwise structure and scale growth in turbulent boundary layers. *Journal of Fluid Mechanics* **490**, 37–74.

Townsend, Albert A 1980 *The structure of turbulent shear flow*. Cambridge university press.

Viswanath, Divakar 2007 Recurrent motions within plane couette turbulence. *Journal of Fluid Mechanics* **580**, 339–358.

Viswanath, Divakar 2009 The critical layer in pipe flow at high reynolds number. *Philosophical Transactions of the Royal Society of London A: Mathematical, Physical and Engineering Sciences* **367** (1888), 561–576.

Waleffe, Fabian 1997 On a self-sustaining process in shear flows. *Physics of Fluids* **9** (4), 883–900.

Waleffe, Fabian 1998 Three-dimensional coherent states in plane shear flows. *Physical Review Letters* **81** (19), 4140.

Waleffe, Fabian 2001 Exact coherent structures in channel flow. *Journal of Fluid Mechanics* **435**, 93–102.

Waleffe, Fabian 2003 Homotopy of exact coherent structures in plane shear flows. *Physics of Fluids* **15** (6), 1517–1534.

Wei, T, Fife, P, Klewicki, J & McMurtry, P 2005 Properties of the mean momentum balance in turbulent boundary layer, pipe and channel flows. *Journal of Fluid Mechanics* **522**, 303–327.

Willis, Ashley P, Cvitanović, P & Avila, Marc 2013 Revealing the state space of turbulent pipe flow by symmetry reduction. *Journal of Fluid Mechanics* **721**, 514–540.

Yang, Qiang, Willis, Ashley P & Hwang, Yongyun 2018 Energy production and self-sustained turbulence at the kolmogorov scale in couette flow. *Journal of Fluid Mechanics* **834**, 531–554.

Yang, Qiang, Willis, Ashley P & Hwang, Yongyun 2019 Exact coherent states of attached eddies in channel flow. *Journal of Fluid Mechanics* **862**, 1029–1059.